Jonni Lehtiranta

Comparison of C- and L-band synthetic aperture radar images for sea ice motion estimation

School of Electrical Engineering

Thesis submitted for examination for the degree of Master of Science in Technology.
Espoo 30.9.2013

Thesis supervisor:

Prof. Risto Wichman

Thesis advisors:

Ph.D Simo Siiriä

D.Sc. (Tech.) Juha Karvonen

Aalto University
School of Electrical Engineering

Preface

The work presented in this master's thesis has been carried out in the Marine Research Programme of the Finnish Meteorological Institute. The main support group was that of Ice Research, splendidly merited in the field of sea ice remote sensing. Being a part of this organization has been inspiring and meaningful, and I am grateful for the opportunity to work in this community.

Special thanks must be extended to professor Risto Wichman of Aalto University who supervised this work with great interest to detail, Simo Siiriä who tirelessly advised all aspects of the research and writing, and Juha Karvonen, whose expert advice and help finding the relevant science were essential in handling the problem.

I'm also very grateful to my superiors Ari Seinä and Eero Rinne who helped in seeing the light, both about the value of this work and at the end of the tunnel, and Patrick Eriksson, who helped in seeing ice-related features in satellite radar images.

A whole lot of thanks and respect goes to my wife Sofia, parents Anna and Jukka, and many friends, who have supported me throughout the challenges I've met while writing this work.

Helsinki, September 30th, 2013

Jonni Lehtiranta

AALTO-YLIOPISTO
SÄHKÖTEKNIIKAN KORKEAKOULU

DIPLOMITYÖN
TIIVISTELMÄ

Tekijä: Jonni Lehtiranta

Työn nimi: C- ja L-taajuuskaistojen SAR-tutkakuvien vertailu merijään liikkeen laskemiseksi

Päivämäärä: 30.9.2013 Kieli: Englanti Sivumäärä:9+49

Signaalinkäsittelyn laitos

Professuuri: Signaalinkäsittely Koodi: S3013

Valvoja: Prof. Risto Wichman

Ohjaajat: FT Simo Siiriä, TkT Juha Karvonen

Merijään liikettä on jo pitkään kartoitettu satelliittitutkakuvien avulla. Käytetyt menetelmät perustuvat kahdesta peräkkäisestä kuvasta havaittujen kohteiden siirtymän laskemiseen. Käyttöön on vakiintunut C-kaista, jolle kuvien saatavuus on hyvä ja joka on merijäälle hyvä kompromissi. 2010-luvulla on käynnissä useita satelliittihankkeita, jotka tuovat käyttöön muiden aallonpituuksien SAR-tutkia. Uudet aallonpituudet ovat lupaavia myös merijään kaukokartoitukseen, erityisesti Itämerellä, ja soveltuvuudesta on tehty useita vertailevia tutkimuksia. Aallonpituuksia ei ole kuitenkaan vertailtu merijään liikealgoritmien näkökulmasta. Tässä työssä verrataan kuvapareja, jotka edustavat C- tai L-kaistaa tai näiden yhdistelmää. Koska satelliittikuvia saadaan kustakin sensorista vain harvoin, eri kuvalähteitä yhdistelemällä on mahdollista saavuttaa parempi ajallinen erottelukyky. Toisaalta eri aallonpituudet ovat perustavanlaatuisesti erilaisia, mikä asettaa työlle erityisiä haasteita.

Tätä työtä varten kirjoitettiin ristikorrelaatioon perustuva algoritmi, jota testattiin C- ja L-kaistan satelliittitutkakuvilla. Työssä ehdotetaan menetelmää näillä aallonpituuksilla Itämerellä toimivaksi jäänliikealgoritmiksi.

Avainsanat: jää,merijää,tutka,itämeri,perämeri,liike

AALTO UNIVERSITY
SCHOOL OF ELECTRICAL ENGINEERING

ABSTRACT OF THE
MASTER'S THESIS

Author: Jonni Lehtiranta

Title: Comparison of C- and L-band synthetic aperture radar images for sea ice motion estimation

Date: 30.9.2013 Language: English Number of pages:9+49

Department of Signal Processing

Professorship: Signal processing Code: S3013

Supervisor: Prof. Risto Wichman

Advisors: Ph.D Simo Siiriä, D.Sc. (Tech.) Juha Karvonen

Pairs of consecutive C-band SAR images are routinely used for sea ice motion estimation. New Earth-observing satellites with SAR instruments of other wavelengths are being introduced. These seem promising for the sea ice regime, especially in the Baltic Sea that lacks multiyear ice and icebergs. In this work, SAR images acquired using different wavelengths are applied for sea ice motion estimation, and the suitability is compared. The work will also investigate motion estimation by using an image pair of different wavelengths. Using images of both C-band and L-band presents more opportunities for calculating motion within a shorter time frame, but presents challenges arising from the fundamentally different nature of reflection in the images.

A motion estimation program was written for this purpose, and a method for calculating sea ice motion from consecutive SAR images, using two images from different frequency bands, is presented. The difficulties arising from differences in wavelength, resolution and reflection characteristics are investigated for sea ice in the Baltic Sea and an algorithm that works for C- and L-band and mixed image pairs is presented.

Keywords: radar,sar,sea,ice,motion,displacement,baltic

Abbreviations and acronyms

ALOS	Advanced Land Observing Satellite
AVHRR	Advanced Very High Resolution Radiometer, a passive multispectral imaging system
c-c	cross-correlation
CPU	Central Processing Unit
ESA	European Space Agency
FFT	Fast Fourier Transform
GDAL	Geospatial Data Abstraction Library
GeoTIFF	Geographic Tagged Image File Format
GPGPU	General Purpose computing on Graphics Processing Units
GPS	Global Positioning System
GPU	Graphics Processing Unit
IFFT	Inverse Fast Fourier Transform
JAXA	Japan Aerospace Exploration Agency
MCC	Maximum Cross Correlation
NetCDF	Network Common Data Format
NOAA	National Oceanic and Atmospheric Administration (of USA)
PALSAR	Phased Array type L-band Synthetic Aperture Radar
RADAR	Radio Detection and Ranging
RAR	Real Aperture Radar
SAR	Synthetic Aperture Radar
WGS84	World Geodetic System 84, a coordinate system standard

Concepts

backscatter	Scattering of a radar pulse from a target towards the radar.
brackish water	Seawater of low salinity; as opposed to oceanic seawater, the temperature of maximum density is above the freezing temperature.
brine	Salt-enriched water found in brine pockets and brine channels inside sea ice.
deformed ice	Sea ice that has broken into separate floes and then rafted on top of each other or formed pressure ridges.
drift ice	Sea ice that moves freely, transported by winds and ocean currents and often deformed to some extent.
incidence angle	The angle between an incoming radar pulse and local vertical direction.
landfast ice / fast ice	Sea ice that is permanently attached to coastal or bottom formations.
lead (sea ice)	Opened linear fractures in an ice cover, revealing open water or newly formed thin ice.
marginal ice zone	Also referred to as sea ice margins, marginal ice zones are transition regions between ice-covered and ice-free portions of the world ocean.
nadir	Direction straight down from the satellite, opposite of the zenith.
noise (imaging)	Random, often granular, error in a satellite image, often caused by electrical noise in the imaging sensor.

Concepts (cont.)

polynya	An area of open water surrounded by sea ice. Polynyas remain ice-free for extended perioids, due to either upwelling of warmer water, or continuous export of formed ice by winds or ocean currents.
pressure ridge	A linear mound of sea ice, formed when pressure forces have forced ice floes to pile up on top of each other (see image 4.2).
swath width	The width of a land area that a radar instrument can record in one go. Depends on the imaging mode used.

Contents

1 Introduction

The Baltic Sea gets an ice cover every winter, covering 45% of its area on an average year. In the northern Bay of Bothnia, the duration of ice cover is from five to seven months, from late October to late May, and the biggest level ice thickness ranges from 50 to 110 cm. Until the 1900th century, ice isolated Finland from the rest of Europe every winter, and regular winter shipping to all important ports became routine in the year 1970. The ice still poses a danger to shipping and forces the Baltic Sea nations to support a fleet of icebreakers. As such, the knowledge of ice conditions is essential for winter navigation. (Myrberg et al., 2006)

Empirical data of the Baltic sea ice is essential to safety in winter navigation. This information is published daily as an ice chart which is based on coastal and ship-based observations and satellite images. Daily sea ice forecasts are also available, predicting parameters like ice motion and compressive forces in the ice pack, both important for navigation and subject to change in a matter of hours. These forecasted values are difficult to validate, because in-situ measurements of ice motion are expensive as motion can only be recorded locally by drifter buoys. Work has been done to calculate ice motion from two consecutive satellite images using optical flow algorithms, and this approach has provided good results using the C-band radar, which represents a good compromise for sea ice remote sensing. In 2010s, there are several projects for introducing new orbital L-band radars. This work will compare C-band with L-band for sea ice motion estimation.

Motion estimation from consecutive satellite images has its limitations however. Only an average velocity can be determined, and that only if the ice surface remained mostly unchanged. Changing weather conditions can change ice surface properties enough to make feature detection impossible, and generally the method only works for image pairs less than three days apart. Previous work has also concentrated on sequential images from a single instrument, which places a limitation on the availability of suitable image pairs. A satellite might fly over the area of interest only once per day or less. For longer time intervals, velocities in short-duration events like storms are lost.

If observations from multiple satellite imaging instruments are considered, image pairs mere hours apart are easier to find, but the benefit comes with the added difficulty of comparing images of fundamentally different character. To improve the situation, this work will examine the idea of calculating sea ice motion using two pictures from different instruments, namely C-band (38 - 75 mm) and L-band (150 - 300 mm) synthetic aperture radars mounted on different Earth-observing satellites.

2 Radar theory for sea ice remote sensing

Remote sensing is the act of obtaining information about the subject of interest through analyzing data acquired by a device that is not in contact with the target (Lillesand et al., 2004). Large scale motion estimation for sea ice was made feasible by the introduction of Earth-observing satellites, and easier by orbital radars that produce clear images regardless of weather. This chapter introduces the reader to remote sensing and synthetic aperture radars, and the properties of different radar wavelengths are investigated.

2.1 Remote sensing using synthetic aperture radar

The act of remote sensing can be thought of as a two-step process of data acquisition and interpretation, the result of which is some useful information. The remotely collected data can be of many forms, including variations in force distributions, acoustic waves and electromagnetic energy distributions. Electromagnetic waves are especially useful as they can be detected far away, react with matter in an astonishing multitude of ways, and are easy to generate and record. Further, the Sun is a continuous source of electromagnetic radiation which allows much imaging to happen purely as passive reception of data. When solar radiation is not available, or when the response to some particular excitation is of interest, man-made electromagnetic radiation is aimed at the target. This is the operational principle of radar instruments (radio detection and ranging) as well, and when microwaves, wavelengths between 1 mm and 1 m, are used, radars can penetrate the atmosphere in all conditions. However, microwave reflections from the Earth's suface are very different from those of visible wavelengths - they are no substitute, but allow a very different view. (Lillesand et al., 2004)

2.1.1 Radar theory

Radar is originally an acronym from "Radio Detection and Ranging". Radars are active devices that transmit a short electromagnetic pulse, and then receive reflections of the pulse at and near the transmitted wavelength. The range of the reflection is determined by the delay of the echo. The power of a returning echo can be calculated using the Radar Equation:

$$P_r = \frac{P_t \sigma_{bs} \lambda^2}{(4\pi)^2 R^4} G_{t,D}(\theta, \phi) G_{r,D}(\theta, \phi) \tag{2.1}$$

where P_r is the received power, P_t transmitted power, σ_{bs} the radar cross section (or scattering coefficient) of the target in square meters, λ the employed wavelength, R distance from radar to target, $G_{t,D}(\theta, \phi)$ the gain of transmitting antenna in the direction of the target and $G_{r,D}(\theta, \phi)$ the gain of the receiving antenna in the target's direction. The radar cross section is the area of a perpendicular surface that would scatter the radar pulse like the target. It depends on the shape, orientation, material and surface of an object and the wavelength and polarization of the radar instrument. (Cheng, 1993)

As the RADAR acronym states, the used wavelength is in the radio part of the spectrum. Radio waves are much longer wavelength than visible light, generally 1 cm and longer. Radar uses a single wavelength for illuminating the desired area, so there is no color information in radar imagery. Instead, additional information can be found in different polarizations, for which radar instruments are generally sensitive for. For radar, the electromagnetic waves are usually polarized in a plane, either horizontal or vertical. (ASAR Product Handbook, 2007)

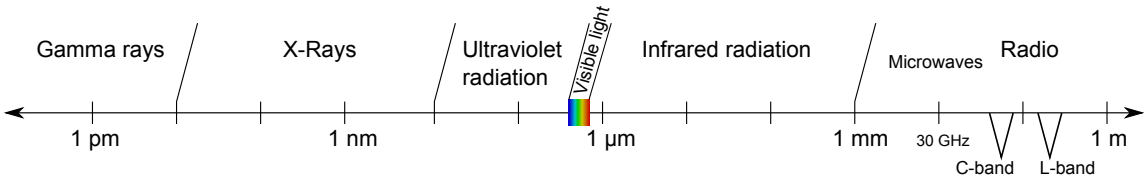

Figure 2.1: Electromagnetic spectrum and radio frequency bands

The wavelengths used range from millimeters to centimeters, and as such, it would be impractical to build an array of imaging elements as in digital cameras. Thus, radars typically have one primary signal receiving unit and the spatial resolution is determined by the shape of the receiving unit and the reflector. Round paraboloid reflectors record a thin beam of radiation, and wide but thin radar units record from a fan-shaped area. Ship radars are of the latter type, and are unable to differentiate between two targets at same range but different altitude.

In imaging applications, the radar is rotated between all desired orientations, and each separate pulse allows recording one line of information, sensing targets on a range of distances in that direction.

2.1.2 Radar backscatter from sea ice

Scattering is the unpredictable diffusion of electromagnetic radiation by particles. Backscatter is scattering caused by a radar pulse back towards the radar instrument. It is the quantity that SAR devices measure. High backscatter will show up in the resulting radar images as bright pixels, low backscatter is represented by darker pixels. As a rule of thumb, higher backscatter represents a rougher surface. In addition to surface roughness, the orientation of surfaces affects backscatter. A surface tilted towards the radar instrument will appear brighter than a surface tilted away from it. Tall formations like mountains can also shadow some areas from the radar instrument and cause them to appear dark. Surfaces that meet at right angles can cause a double-bounce, directing the radar pulse directly towards the antenna via two specular reflections, and cause a very bright echo. (ASAR Product Handbook, 2007)

Sea ice is a complex material consisting of a variety of ice crystals, brine channels and pockets, air bubbles and snow. In sea ice, there is ample opportunity for scattering, both from surface features and scatterers inside the ice volume. The surface scattering depends on surface roughness and wetness of ice and possible snow cover. It is also sensitive to the orientation of surfaces - a corner reflection from two nearly perpendicular surfaces can cause a strong reflection, an order of magnitude brighter than surrounding backscatter. High backscatter implies a large number of broken pieces in the area. Volume scattering, happening inside the solid volume of ice, additionally depends on salinity, the crystal structure and snow cover. The depth of volume scattering in the Arctic is in the order of a few centimeters for C-band radar, more for L-band. It is controlled by the interplay of radar wavelength and the dielectric constant of the material, which for sea ice depends strongly on the amount of brine and air pockets in the ice. It is additionally affected by radar polarization and view angle. Generally new, young ice has more air and brine inclusions, but the amount of brine also changes with the ice temperature. In cold ice, some of the brine freezes, leaving behind smaller amounts of more saline brine, and this process reverses when the ice warms up again. Salinity of new ice is about half that of seawater, and decreases with time (Leppäranta, 2011). Brine pockets are an impediment to electromagnetic signals, so deepest penetration is found in dry ice of low salinity. Near sea ice, there is often open water and some backscatter will also be received from a water surface. In cold oceans, open water is found in leads and polynyas and beyond the ice margin. The backscatter is very small from calm water, and in this case it's easy to distinguish water from ice. However, a breeze can

roughen the water surface and produce waves. Backscatter from waves is generally brighter than that of sea ice when wind speed exceeds 4-5 m/s. (Johannessen et al., 2007)

2.1.3 Synthetic aperture radars

In conventional radars (Real Aperture Radars, RAR) antenna size must increase in proportion with the desired image resolution. For spaceborne radars this is a serious limitation. With Synthetic Aperture Radars (SAR), it is possible to achieve a spatial resolution of 10 meters or better. Like conventional radars, SAR instruments are largely unaffected by weather conditions (ALOS User Handbook, 2007). The SAR instruments achieve this high resolution by recording radar echoes during orbital motion, and synthesizing large-antenna behavior by using the doppler history of the echoes. While the radar footprint is in the order of 5 km, upshifted echoes from ahead of the SAR instrument can be discerned from echoes from the downshifted echoes from behind. Both the amplitude and phase of returned signals must be recorded, and the final image is constructed through intricate calculations. (ASAR Product Handbook, 2007)

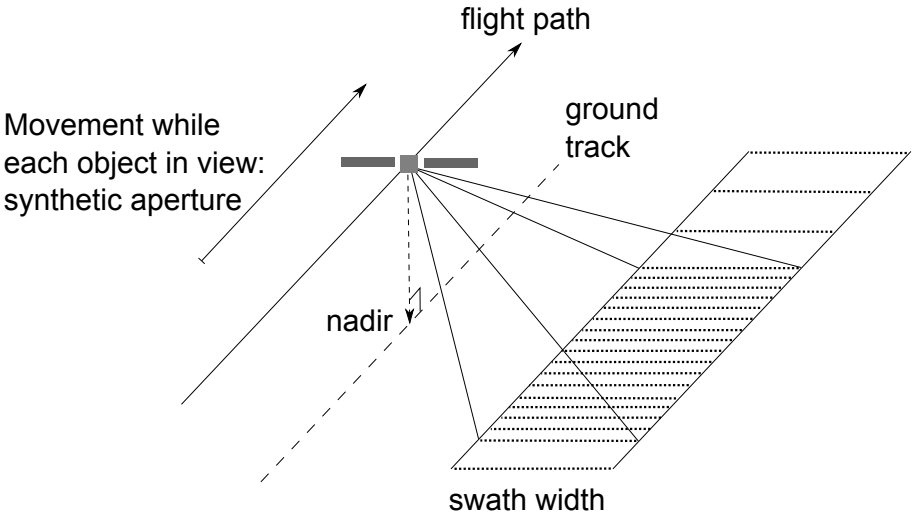

Figure 2.2: Imaging geometry for orbital SAR instruments

2.1.4 Imaging geometry for orbital SAR

Radar antennas for Earth observation are generally mounted on aircrafts and spacecrafts. These transmit a radar signal in a side-looking direction, hitting Earth's surface far away from nadir (ASAR Product Handbook, 2007). This is because a

radar system can only distinguish between echoes by their delay and phase. This means that a radar pulse hits scattering targets at varying distances and angles. The angle between the radar pulse and Earth surface's normal is called the incidence angle. The varying incidence angle presents many difficulties to image interpretation. One advantage of smaller incidence angles is that terrain distortion is reduced.

2.1.5 SAR image polarization options

Imaging radars can transmit horizontally (H) or vertically (V) polarized electromagnetic pulses. Regardless of the polarization of the transmitted signals, radars can record horizontally or vertically polarized echoes or both. Generally the strongest echoes are polarized the same way as the transmitted pulse, as simple surface and volume scattering preserve the polarization. Multiple scattering, for example from a volume or rough surfaces, can produce a cross-polarized echo. VV polarization (Vertical transmit and Vertical receive) is the preferred configuration in a number of applications including the study of small-scale roughness of waves on water surfaces. HH polarization is more useful for separating sea ice from water, since it's less sensitive to waves. HH polarization is also sometimes preferred for its better penetration through vertically oriented stalks of crops. Cross-polarization (VH or HV) is especially good for detecting targets on the water surface, including ships and deformed sea ice. (ASAR Product Handbook, 2007)

SAR imaging instruments offer a choice between different polarization modes, and more recent instruments offer a fully polarimetric mode which records backscatter for all combinations of transmitted and received polarizations: HH, HV, VV and VH. Fully polarimetric imaging is only available for images of small coverage, as wide SAR images are composites of several imaging beams, which are then not available for polarimetry. For sea ice mapping and motion estimation purposes, only single-polarization modes are feasible. Forming an image comprising of several imaging beams is challenging, and visible edges can appear in pictures using wide imaging modes.

2.2 Sea ice information from C- and L-band radar

Sea ice remote sensing has traditionally used space-borne C-band SAR, which is regarded as a reasonable choice for generic sea ice work. For some tasks, however, other frequency bands may be more suitable. The suitability of a SAR sensor for a specific task depends on its swath width, spatial resolution, frequency, incidence

angle and polarization. SAR satellites tend to differ from each other in all of these details, and a one-to-one comparison of SAR frequency bands is unavailable. It is known, that reflections are generated only when reflecting surfaces are larger than the radar wavelength (Eriksson et al., 2010). Shorter wavelengths produce more surface scattering and reflect strongly from small-scale surface roughness, while for longer wavelengths the backscattered signal is less sensitive to small-scale roughness and small scatterers. As the longer wavelengths penetrate deeper, they are less sensitive to moisture and other surface features that might mask more relevant details. (Johannessen et al., 2007)

	Frequency range	Wavelength range
L	1 - 2 GHz	15 - 30 cm
C	4 - 8 GHz	3.75 - 7.5 cm
X	8 - 12 GHz	2.5 - 3.75 cm
Ku	12 - 18 GHz	1.67 - 2.5 cm

Table 1: Radar bands used in sea ice research

For comparing different radar setups, a number of studies dealing with sea ice signatures have been carried out. SAR instruments have been tested on ground level, mounted on airplanes and on satellites. Dierking and Busche provide an extensive assessment of comparisons done prior to 2006. According to them, many researchers have reported that at L-band, the contrast between ice types is very small but that pressure ridges are easier to distinguish. It is also widely reported that L-band has an advantage during melt season, due to its larger penetration depth, and that the contrast between deformed and level ice types is clearer (Onstott, 1992). However, the L-band performs worse than shorter wavelengths in areas with scarce deformation features, and C-band is more reliable for detecting melt and freeze-up events. For most other purposes, reports differ on their conclusions. Dierking and Busche propose that this might depend on different data analysis methods, and that an advanced analysis of multi-polarization L-band data would be more accurate for overall classification than C-band. If only one polarization is available, L-band is judged to be a secondary choice for ice classification. The comparison is problematic though, as all SAR instruments differ from each other in other details as well, instead of just the frequency band, and no real one-to-one comparison could be made. They summarize that during winter months, short wavelengths (X- and Ku-band) are desirable, C-band is a good compromise, and L-band is suitable for warmer months. (Dierking and Busche, 2006)

Some work has also been done to assess the ALOS PALSAR L-band images

	Advantages	Disadvantages
C-band	Reliable detection of melt and freeze-up events Good contrast between first-year and multiyear ice	Poor performance after the onset of surface melting
L-band	Contrast between level ice types is small Poor detection of multiyear ice and icebergs	Pressure ridges easy to distinguish Good contrast between level and deformed ice More capable during melt season

Table 2: Summary of advantages and disadvantages of C- and L-band SAR for sea ice monitoring

for sea ice as compared to RADARSAT-1. The Canadian Ice Service compared PALSAR's images of sea ice to RADARSAT-1 images. They report that PALSAR images contain a far superior amount of ridge information compared to C-band images. Large ridges are clearly defined, and this detail remains in images well into June, when surface melting causes problems for C-band images. L-band images also still clearly delineate separate ice floes while C-band images appear "washed out" and hopeless for floe edge detection. They also report that PALSAR allows thin ice to be easily distinguished from thick ice, while C-band images could confuse rough thin ice with thicker ice types. However, multi-year ice, while visible in L-band images, is almost indistinguishable from first-year ice and the contrast between an iceberg and the surrounding pack ice is much weaker than in C-band images. (Arkett et al., 2008)

Additionally, Eriksson et al. compared several SAR satellite products on the Baltic sea. The area differs from Canadian arctic by its very low water salinity and lack of multiyear ice and icebergs. Comparing ALOS PALSAR with Envisat ASAR, RADARSAT-2 and TerraSAR-X, operating on X-band, they report that X-band is largely equivalent to C-band in practice while L-band is markedly different. They note that in all evaluated SAR bands, landfast ice appears bright and new ice appears dark. Their work supports the conclusions of Arkett et al., not adding much except evidence that the Arctic and the Baltic oceans are similar in terms of remote sensing by SAR. (Eriksson et al., 2010)

3 Sea ice motion estimation using satellite images

The distribution of apparent velocities of movement of patterns in an image is called *optical flow*. Motion, as estimated from consecutive images, is an apparent transportation of some pattern. It's a vector quantity measured in pixels. In a photograph, actual objects fall in a range of distances from the camera, and the pixels don't represent anything particular. For our purposes, and typically for Earth observation data, charts etc., a one pixel distance roughly equals a real distance depending on the projection.

The first scheme for automatically calculating optical flow was presented by Horn and Schunck. They approached the problem by defining image brightness $E(x, y, t)$ and assuming that the brightness of a particular point in the pattern is constant, so that

$$\frac{dE}{dt} = 0 \tag{3.1}$$

so that the total derivative is

$$\frac{\partial E}{\partial t} + \frac{\partial E}{\partial x}\frac{\partial x}{\partial t} + \frac{\partial E}{\partial y}\frac{\partial y}{\partial t} = 0.$$

While the change of brightness between two images is known, the x- and y-velocities present two unknowns. The needed additional constraint proposed is the requirement that movemet must be continuous in a set of images. (Horn and Schunck, 1981)

This approach presented several limitations including the assumption of constant illumination and image smoothness and the requirement of small displacements between images. Work has been done to alleviate these problems (eg. Anandan and Weiss, 1985; Nagel and Enkelmann, 1986), and several modern methods are presented in (Kim et al., 2005). Despite improvements, these methods have not been applied in the realm of sea ice.

3.1 Sea ice motion estimation

Remote sensing of sea ice motion started with sequential optical images from airborne and spaceborne platforms. At first this was done by a human operator, who would identify features in an image of a sea-ice field to use as "tie points", and then find the same features in subsequent images on a split-screen video display (Hall and Rothrock, 1981). After hand-picking these points, ice velocity was calculated

automatically. Even so, this process was too slow and expensive for real-time analysis or extensive work, and the introduction of several Earth-observation satellites necessitated the development of fully automated techniques (Vesecky et al., 1988).

Optical satellite images suffer from cloud cover and other weather issues, and imaging radars were soon employed as these provide a high resolution and weather independence. Synthetic aperture radar (SAR) satellite images in particular have been analyzed with several algorithms (eg. Collins and Emery, 1988; Vesecky et al., 1988; Liu et al., 1997; Karvonen et al., 2007; Thomas et al., 2011). More recently, also passive microwave data from earth observation satellites has been employed. These devices have had daily coverage for both poles since 1978 (nsidc.org), which provides long time series and makes these data useful for climatological investigations. (Leppäranta, 2011)

3.1.1 Automated methods: cross correlation

In 1986, Ninnis, Emery and Collins described an automated technique for computing ice motion. Their technique was based on cross-correlating two small square windows of the sequential images. For these windows, consider two signals $f(x, y)$ and $g(x, y)$. These are related by a vector displacement (x_0, y_0).

$$f(x, y) = g(x + x_0, y + y_0) \tag{3.2}$$

The cross-covariance function was defined by

$$r_{fg}(x', y') = E\left[(f(x, y) - m_f)\left(g(x + x', y + y') - m_g\right)\right] \tag{3.3}$$

where $E[]$ is the expected value and m_f, $m_g$are the signal means. The normalized cross covariance is given by

$$\rho\left(x', y'\right) = \frac{r_{fg}\left(x', y'\right)}{\left(\sigma_f^2 \sigma_g^2\right)^{1/2}} \tag{3.4}$$

where $\sigma_f$and $\sigma_g$are variances of f and g. For finding the relative displacement, it is sufficient to find the vector displacement that maximizes the cross-correlation function. This computation was done in the frequency domain to achieve speed benefits using the circular convolution theorem: an algorithm using FFTs has a computational complexity $O(n\,log\,n)$ instead of $O(n^2)$. The window sizes employed were $22x22$ for $f(x, y)$ and $32x32$ for $g(x, y)$, chosen such to avoid problems from correlation wrap-around. This Maximum Cross Correlation (MCC) method was ap-

plied to all chosen window pairs, the result being an array of displacement vectors. This method was successful at estimating ice motion using AVHRR images, as compared to buoy movements and known wind conditions in the eastern Beaufort sea (Ninnis et al., 1986). The Advanced Very High Resolution Radiometer (AVHRR) is a passive imaging device that works on several frequency bands of red, near infrared and thermal infrared. Its spatial resolution is about 1 km, and its images suffer from changing weather conditions

Emery et al developed filters for cloud detection and removal and other purposes and used overlapping windows to achieve a tighter vector field. They successfully applied their method to the Fram strait, choosing to calculate the cross-correlation directly from image brightnesses rather than using FFTs and the circular convolution theorem. They did this because the direct method allows greater flexibility in varying the computational parameters. The straightforward calculation also allowed them to estimate ice motion near coastlines, where windows of irregular shape are required. Chosen window sizes were $55x55$ for the search window and $15x15$ template windows. In the used form, the MCC technique assumes a linear displacement and fails to work correctly when ice floes rotate or deform. (Emery et al., 1991)

Other studies (Fily and Rothrock, 1987; Collins and Emery, 1988) applied the maximum cross correlation technique to synthetic aperture radar images. Due to the synthetic aperture technique, these images have a higher resolution and higher demands for storage and computation. To alleviate the increased requirements, Fily and Rothrock introduced an optimization that first calculates large-scale average motion from coarse images and uses this result as an initial guess on each level of the pyramid of progressively higher-resolution data (Fily and Rothrock, 1987). Fily and Rothrock calculated cross-correlations directly in the spatial domain, and Collins and Emery used the fast fourier transform (FFT) for the task a year later. They also report that using a two-stage matched filter that is practically equivalent to an edge detection step reduces both the number of errors and their magnitude (Collins and Emery, 1988).

3.1.2 Feature tracking

In 1988, Vesecky et al looked into motion detection using feature tracking on Seasat SAR images. The feature tracking approach consists of detecting some features in two satellite images, and then matching the detected sets of features. They implemented a method that detects and then tracks floe-lead boundaries. The ice-water boundaries were selected amongst a wide variety of trackable features as they are

usually most prominent, distinct and high-constrast features in SAR images of sea ice, and could be found using edge detection. Pixels on the edge are assembled into boundary segments, a dominant boundary direction is calculated, and segments are characterized by their deviations from straight lines. Matching features are then found by comparing the sets of deviation measurements using variance-normalized cross-correlation. They also compared feature tracking with a cross-correlation method, conclude that both methods function well while having distinct strengths and weakness, and propose an algorithm synthesized from both techniques. (Vesecky et al., 1988)

While the first methods were successful in the central ice pack, where rotation of ice floes would be minimal, Kwok et al suggested an algorithm that would work even in the coastal and marginal ice zones where rotations are commonplace. They achieved this goal by using a hybrid approach which combined feature tracking with area-based cross-correlation. For the central ice pack, cross correlation was done to image windows in steps of low-resolution and high-resolution windows. For ice margin, they first extracted distinct features with a high probability of successful matching, matched them, and did a filtering step. This would provide a sparse estimate for both displacement and rotation. The final movement was calculated by cross-correlating high-resolution windows that were rotated according to the rotation angles produced in the previous step. The matched features in this work were region boundaries. A region was defined as a connected image area exhibiting similar attributes in terms of brightness and texture. In practice, these regions could be ice floes or areas of similar ice type, or open water. The regions were formed automatically by a clustering of image attributes, and a boundary was calculated for representing the shape of each region. Boundaries were vectorized and transformed to one-dimensional $\psi - s$ curves that relate the direction of the boundary with displacement from an arbitrary starting point along the boundary. In this representation, any rotation of a region is represented by a displacement of the $\psi - s$ curve. Features were matched by 1-dimensional cross-correlation of these boundary curves. This method was verified using SEASAT L-band images and tested with C-band images captured by an airborne sensor. (Kwok et al., 1990)

3.1.3 Methods specific to fourier transformation

An algorithm using power spectra to estimate rotation in addition to translation was proposed by Yan Sun. He presented the algorithm for matching two entire images in order to produce an estimate of global movement. For finding the rotation

between images, the 2-dimensional power spectra of the images would be considered. The power spectra ignore translation, but depend on rotation which can be derived from them by cross-correlation. In 2-dimensional FFT, the frequency space values represent components with amplitude, wavelength and direction. After discarding very low-frequency values, which are not sensitive to small rotations, and very high-frequency values, which are mainly noise, relevant information resides on an annulus. These are projected on a rectangular array in order to use ordinary image processing software. The rotation angle becomes a translation, and is calculated using cross-correlation. The angle is used to rotate one of the input images, after which translation can be found using cross-correlation. (Sun, 1994)

Phase correlation has also been applied to ice motion estimation of the Baltic sea (Karvonen et al., 2007; Karvonen, 2012). This method optimizes the robustness of detecting the correlation maximum at the expense of increased sensitivity to noise, to which it is more sensitive than direct cross-correlation (Manduchi and Mian, 1993). Phase correlation exploits the affine Fourier theorem, useful for speeding up cross-correlation calculations, and introduces an additional step in frequency space. After applying a 2-D FFT to data windows, all FFT coefficients are normalized by their magnitudes and then multiplied together. While a cross-correlation result generally has multiple peaks, the IFFT of the "whitened" signals theoretically produce a Dirac delta function centered at the translation parameters (Thomas, 2004).

3.1.4 Tracking of ice edges by wavelet analysis

Liu, Matrin and Kwok introduced a method for detecting and tracking ice edges and ice floes by wavelet analysis of SAR images. Their subject of study was the development of polynyas, open water areas, in an ice-covered region. A mexican hat wavelet is used to transform the images, and edges are found using the contours of zero crossings. They first use a large-scale wavelet to find an approximate boundary in ice, and then use a small-scale wavelet to find areas in the vicinity of the large-scale boundary. Found small elements are linked through their centers of mass to give an accurate representation of the whole ice edge. The method is reported to work well even when liquid water, present on top of ice, reduces backscatter, and both rotation and translation can be calculated efficiently (Liu et al., 1997).

3.1.5 Composite methods

To develop motion tracking and solve the problems caused by discontinuities and deformation, composite methods have been developed. Thomas, Kambhamettu and

Geiger improved upon previous work by building a cascaded motion tracking framework. It begins with a coarse resolution image and works its way towards progressively more accurate motion estimates. On each step and for each block of pixels, motion candidates are found based on peaks in phase correlation. One of these candidates is selected based on normalized cross correlation and accuracy is further improved to sub-pixel level using a three-point Gaussian interpolation. Then, the motion field is smoothed by propagating motion computed for continuous regions to regions that were flagged as discontinuities. The search area is smaller on each successive resolution. (Thomas et al., 2011)

3.2 Vector median filtering

After calculating the motion vector field, typically lots of spurious errors remain among the correct motion vectors. A common method for removing the errors is to use vector median filtering (Vesecky et al., 1988; Karvonen et al., 2007), which replaces each vector with the median vector of its neighborhood. Thus wrong values are replaced with ones most typical for that area. As erroneous vectors are often extreme and very different from the rest of the field, they are often removed by the median filtering even if only a minority of local motion vectors are correct.

Further, median filtering will preserve edges and smooth gradients in the vector field, preserving these often realistic features. For filtering impulsive noise, the median filter has the advantage of selecting between input values, a useful property that cannot be found in linear filters.

The median of N scalars $x_i, i = 1, ..., N$ can be defined as the value x_{med} such that for all y, $y \in x$,

$$\sum_{i=1}^{N} |x_{med} - x_i| \leq \sum_{i=1}^{N} |y - x_i| \tag{3.5}$$

A conventional median filter, which picks the centermost value of some window of scalars, is not straightforward to generalize to n-dimensional vector data. Median-filtering vector components separately can distort the signal, as output vectors are generally not chosen from the input vectors and this procedure ignores the code-pendency often found in real vector signals. Thus, different median-like operations have been proposed, originally by Astola et al. They required a vector median-like method to have the following properties:

- The filter's impulse response is zero

- The filter is robust and well suited for filtering out noise of unknown characteristics
- A step-like edge is retained by the filter
- The vector median filter reduces to scalar median when the vector dimension is 1
- The output vector value is one of the input vectors.

Astola et al approached the problem by assuming the samples come from a density function with an unknown location parameter. Given a random sample $\{x_1, ..., x_N\}$, a maximum likelihood estimate is calculated for the location parameter. When the density function of a Laplace distribution is chosen (sometimes called biexponential or double exponential as the probability density falls exponentially on both sides), this maximum likelihood estimate is equal to the median of $\{x_1, ..., x_N\}$. This is similar to the average being a maximum likelihood estimate for the Gaussian distribution. This approach yields to n-dimensional data, given some reasonable assumptions. They give two different vector medians VM_{L2} and VM_{L1}, which differ only by the usage of L2 vs L1 -norm depending on the assumed noise characteristics. L1-norm (also called Manhattan norm) is a distance- or error-metric defined as $\sum |x_i|$. L2-norm (also called Euclidean norm) is a distance- or error-metric calculated using the Pythagorean theorem. When noise in different vector components is not independent, the L2-norm is used and the vector median is defined as such:

$$\overrightarrow{x_{vm}} \in \{\overrightarrow{x_i} | i = 1, ..., N\} \tag{3.6}$$

and for all $j = 1, ..., N$

$$\sum_{i=1}^{N} \|\overrightarrow{x_{vm}} - \overrightarrow{x_i}\|_2 \leq \sum_{i=1}^{N} \|\overrightarrow{x_j} - \overrightarrow{x_i}\|_2 . \tag{3.7}$$

As can be seen, this is similar to the scalar equation 3.5. A straightforward algorithm for finding the vector median involves calculating distances to all other vectors for every vector, and choosing the vector for which this sum is minimized. (Astola et al., 1990)

4 Employed SAR instruments and Baltic sea ice

This chapter gives in-depth information about the different synthetic aperture radar instruments used in this work. It also describes the features of sea ice that are expected to appear on the baltic. This information allows the interpretation of SAR images on the Baltic.

4.1 Satellites and Instruments

In this work, radars of two different frequency bands will be used, namely C- and L-bands. There are several C-band instruments in operation as of 2013. Currently there are no L-band radars orbiting Earth despite several Japanese satellite missions having carried the technology. Fortunately, the ALOS-2 satellite is planned for launch during 2013, and will carry an improved L-band SAR instrument (Kankaku et al., 2009).

4.1.1 Envisat ASAR

Envisat was an Earth-observing satellite launched by ESA in 2002 and operating until 2012, when communication to the satellite was lost (Dierking and Haas, 2012). Already prior to that, in 2010, the Envisat mission was forced to change strategy and cease the orbit inclination control to save rocket fuel, as the Envisat had outlived its planned mission lifetime of five years (Miranda et al., 2010). The Envisat was designed to provide continuity to the ERS SAR operations, which carried C-band SAR instruments and were operated in years 1991 - 2000 (ERS-1) and 1995 - 2011 (ERS-2). It provided C-band (5.331 GHz) dual-polarization SAR images, offering two channels of image information in three optional configurations. Envisat orbits the Earth in the altitude of 785 kilometers on a polar orbit, and completes one orbit approximately every 101 minutes. The instrument's range of incidence angles ranges from 15° to 45°. (ASAR Product Handbook, 2007)

4.1.2 Radarsat-2 SAR

RADARSAT-2 is a canadian commercial SAR satellite that was launched in 2007 to support and eventually replace the work of the older RADARSAT-1, which was launched in 1995 and operated until March 2013. Both satellites are on polar, sun-synchronous orbits with a perioid of approximately 101 minutes. The radar instruments onboard RADARSAT-2 operates on the C-band (5.405 GHz) and pro-

duces images in four different polarization settings. Its spatial resolution is 3 - 100 meters depending on the imaging mode. For the ScanSAR wide imaging mode most useful for mapping in the scale of the basins of the Baltic Sea, the incidence angle is between 20 - 49 and the image width is nominally 500 kilometers. (Morena et al., 2004)

4.1.3 ALOS PALSAR

The japanese Advanced Land Observing Satellite was launched in 2006, and lost all power through malfunction in April 2011. It houses three remote-sensing instruments; the panchromatic stereo matting instrument PRISM, the Advanced Visible and Near Infrared Radiometer AVNIR-2, and the Phased Array type L-band Synthetic Aperture Radar which is used in this work. ALOS was launched into space by JAXA from the Tanegashima Space Center in Japan, the first PALSAR image being acquired on 14. February, 2006. After that, the instrument was calibrated, detailed characterization of the sensor data was conducted, processing algorithms were designed and image processing software were developed and optimized. After the evaluation period, distribution of standard data began on October 24, 2006. It orbits the Earth at an altitude of 691.65 km on a sun-synchronous sub-recurrent orbit with a repeat cycle of 46 days and an inclination of 98.16 degrees. The center frequency for the L-band operation is 1270 MHz, and while the instrument was capable of various custom imaging modes, three standard modes of operation have been chosen. Due to its orbit, PALSAR could not observe areas beyond 87.8 deg. north latitude and 75.9 deg. south latitude, when the off-nadir angle is 41.5 degrees. (ALOS User Handbook, 2007)

4.1.4 Roundup of the instruments

All the employed SAR instruments support several imaging modes offering a choice of resolutions, polarizations and swath widths. Typically the higher resolutions are provided in narrower image widths, and for wide imaging modes, polarization options are limited. This is because wide SAR images are typically composites using several imaging beams, which are then not available for polarimetry. For sea ice mapping, a wide image area is used.

Instrument	EnviSAT ASAR	RADARSAT-2	ALOS PALSAR
imaging mode	Wide Swath	ScanSAR wide	ScanSAR
polarization	HH or VV	HH+HV or VV+VH	HH or VV
swath width	405 km	500 km	350 km
resolution	150 m	100 m	100 m
incidence angle	15 - 45	20 - 49	18 - 43
frequency	5.331 GHz	5.405 GHz	1.270 GHz

Table 3: Details of the SAR instruments for the wide imaging modes used in this work.

4.2 Sea ice on the Baltic

This subsection will describe the features we expect to see in the Baltic Sea during winters. First, the annual and inter-annual variability of sea ice is described, then ice as a material will get a closer view. Third, the possible snow cover features are examined, and finally the ice movement and resulting deformation events and shapes are discussed.

4.2.1 Sea ice extent on the Baltic Sea

The Baltic Sea experiences a cycle of partial freezing in the winter and full melting during spring and summer. Multiyear ice is completely absent. The severity of winters is classified by the maximum ice extent of each year. By the widely used classification of ice winters by Seinä and Palosuo (1996), mild, average and severe winters each contain a third of the winters in the perioid 1720-1995 (Seinä et al., 1997) :

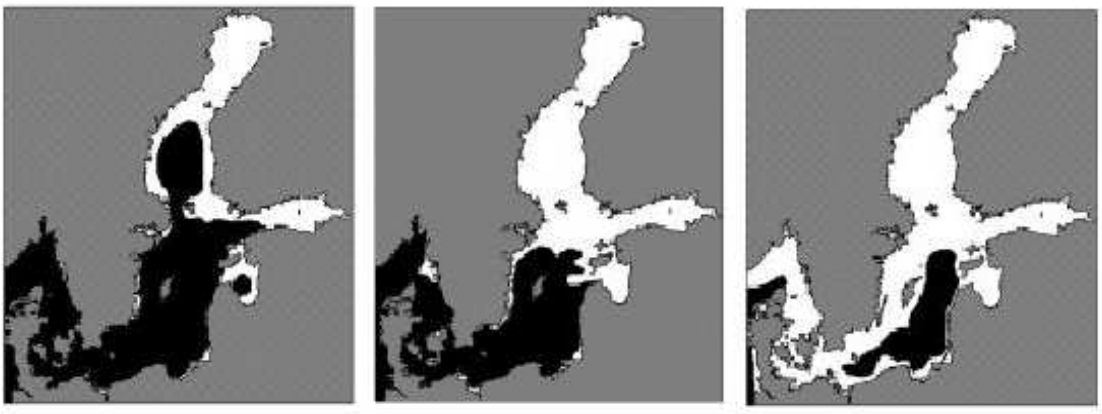

Figure 4.1: Ice cover maximum on mild, normal and a severe winter according to Seinä and Palosuo (1996)

Typically freezing begins on the coast of Bothnian Bay in early November and on the Gulf of Finland a month later. Although the interannual variability in ice conditions is large, a trend towards smaller ice cover is detected during the latter half of the 19th century. Measurements of drift ice thickness are lacking, and the total mass of sea ice in the Baltic and its climatic change are still poorly known. (Vihma and Haapala, 2009)

4.2.2 Growth and structure of sea ice

During the summer the seawater warms up and stores heat. Towards the winter, the cold air cools the seawater towards the freezing point. During this cooling, a vertical circulation, convection, mixes the water down to the depth of the thermocline, below which the waters are always cold. (Weeks and Ackley, 1986) Consequently the shallower areas are likely to freeze up first, and this is what is usually observed on the shallow coastal areas. Laterally, the sea ice is divided into *landfast ice*, frozen to the shoreline, and *drift ice* which is pushed around by winds and currents and thus experiences deformations.

The baltic sea is a body of *brackish* water. That means it has moderate salinity, but the freezing point temperature remains lower than the temperature of maximum density, unlike the oceanic seawater for which these temperatures are the same (Frisk et al., 2003).

Sea ice has two possible directions for growth. Downward, ice crystals grow steadily as long blades and form strong, relatively clear *congelation ice*. Upward, liquid water from rain, snowmelt or flooding freezes to create a darker, uneven layer of *slush ice*. While the freezing process extracts salts to the seawater underneath, some saline water is trapped within the ice inside *brine pockets*. Gas bubbles also exist, especially in the slush ice layer.

4.2.3 Snow cover

For much of the time, sea ice is covered in snow. Consequently, the usual surface that can be observed is snow, not ice. The snow cover is a complex structure in itself, consisting of layers created by distinct events of snowfall, rain, wind drifting, melting and refreezing. The deposited snow will also grow denser with time even without outer influence as it compacts under the influence of gravity. (Eicken et al., 2009)

The snow cover acts as a layer of insulation limiting the growth of sea ice. In the Bay of Bothnia, its importance is on par with the coldness itself, usually measured

in freezing-degree-days, and must be accounted for in any model for thermodynamic ice growth. The ice might well be thicker in a mild but snowless winter compared to a severe winter with lots of snowfall.

The snow cover is in a constant change. Heavy snowfall can renew the visible surface in the matter of hours, and heavy winds can disperse the snow cover even faster. Much of the snow can sublimate under the right conditions, but more typically some of the snow will melt on warmer days, providing water that can freeze again on top of the more saline sea ice. The changes of liquid water content are especially important for radar backscatter.

Dry snow is essentially transparent in C-band radar images, but wet snow produces a moderate echo. If wet snow refreezes into coarse crystals, these will cause a strong backscatter in C-band SAR (ASAR Product Handbook, 2007). The high attenuation of wet snow reduces the contrast between level and deformed ice (Mäkynen and Hallikainen, 2004).

4.2.4 Ice drift

On the northern hemisphere, average velocities of ice drift are 1 - 5 cm/s, but speeds exceeding 1 m/s are possible. Most of the time the ice drift is wind-driven, velocities averaging 2.5% of the wind speed. The ice drift direction is 20° right from the wind direction due to Coriolis effects. However, occasionally the internal friction of ice causes unexpected sudden changes in its movement. A rare, extreme case is the *ice river* phenomenon, limited to coastal areas, that can cause a narrow band of sea ice flow at speeds up to 3 m/s and far faster than the surrounding ice field. The typical rotation rate of ice floes in the Arctic is about $0.2°/h$, the rotation rate increasing in less compact ice. When ice was compact (coverage over 85%), the ice floes rotated less, and tended to rotate as groups instead of individually. (Leppäranta, 2011)

4.2.5 Deformations

Especially in the drift ice zone, sea ice typically undergoes numerous deformation events before eventually melting. These are initiated with the breaking of ice, caused by waves, sea level changes, ship passage and storms, and completed with piling up of ice floes thus created. Thinner ice experiences rafting, where two floes can slide on top of each other, and ridging, where blocks of ice pile up randomly to make linear formations which align themselves perpendicular to compressive stress. Such *pressure ridges*, an example seen in figure 4.2, are typically between 5 and 15 meters thick (Leppäranta and Hakala, 1992). Over large areas, their volume may account

Figure 4.2: An ice ridge partially covered in snow on the Baltic Sea near Kokkola.

for up to one half of the total ice volume. Most of the mass under the water level in the *ridge keel* and occationally all the way to the bottom of the ocean. In hydrostatic equilibrium, the corresponding *ridge sails* visible above the surface are at most a couple of meters high. The length of a ridge can be many kilometers. As the ridge sail is a protruding, irregular jumble of blocks of ice, the pressure ridges are the most remarkable features in ship radars and readily visible from space as well (Leppäranta, 2011).

The deformation events themselves happen at short time scales, typically when storms cause strong winds. Between these events the ice itself remains unchanged. These events make motion estimation challenging near the deformations, which appear as discontinuities in the motion field (Thomas et al., 2011).

5 Materials and methods for motion estimation

In this chapter, the processed SAR images and prevailing conditions for the chosen time perioid (16. - 18. March, 2009) are presented. Also the applied image enhancing methods and the motion estimation approach are described and the study problem is formulated in detail.

For this work, a set of SAR images from March 2009 were used. C-band images were available from both EnviSAT and RadarSAT, while L-band images were available from ALOS PALSAR. A set of six images were chosen for the time period between 16. and 18. March. These days were chosen because there were relatively many images available, including two L-band images, and the latter L-band image (image 6 in 5.4) coincides very well with the C-band image 5. Also, lots of changes including compaction and lead opening were present during this period. Landfast ice and open water areas were seen in visual inspection, and all possible kinds of winter ocean environments were present in this limited set of images from just the Bay of Bothnia. The small ice-covered parts of the Gulf of Finland were judged to be both inconsequential and challenging in the set of images that were available for this work.

5.1 Regions and observed real events

The area of interest is the northern part of the Baltic Sea. At that time, the Bay of Bothnia was mostly but not completely ice-covered. As the ice cover in other parts of the Baltic was sparse, the studied region was limited to the northern side of the 63th parallel, approximately the latitude of Vaasa. This means that the topographical regions in question are the Bay of Bothnia, which is the northest basin of the Baltic Sea, and Kvarken, a shallow strait which separates it from the rest of the sea. The Bay of Bothnia is relatively shallow, with average depth of 41 meters, and gently sloping in the eastern and northeastern coasts, which typically have large areas of landfast ice. (Myrberg et al., 2006)

During the 16th and 17th March the ice pack was moving and compacting towards the north, but the flow direction changed abruptly and in the 18th day images much of the ice had returned southwards, and we see the formation of new ice leads, dominantly in an east-west direction near the edge of landfast ice. In addition to moving back and forth, the dynamic ice edge changed shape.

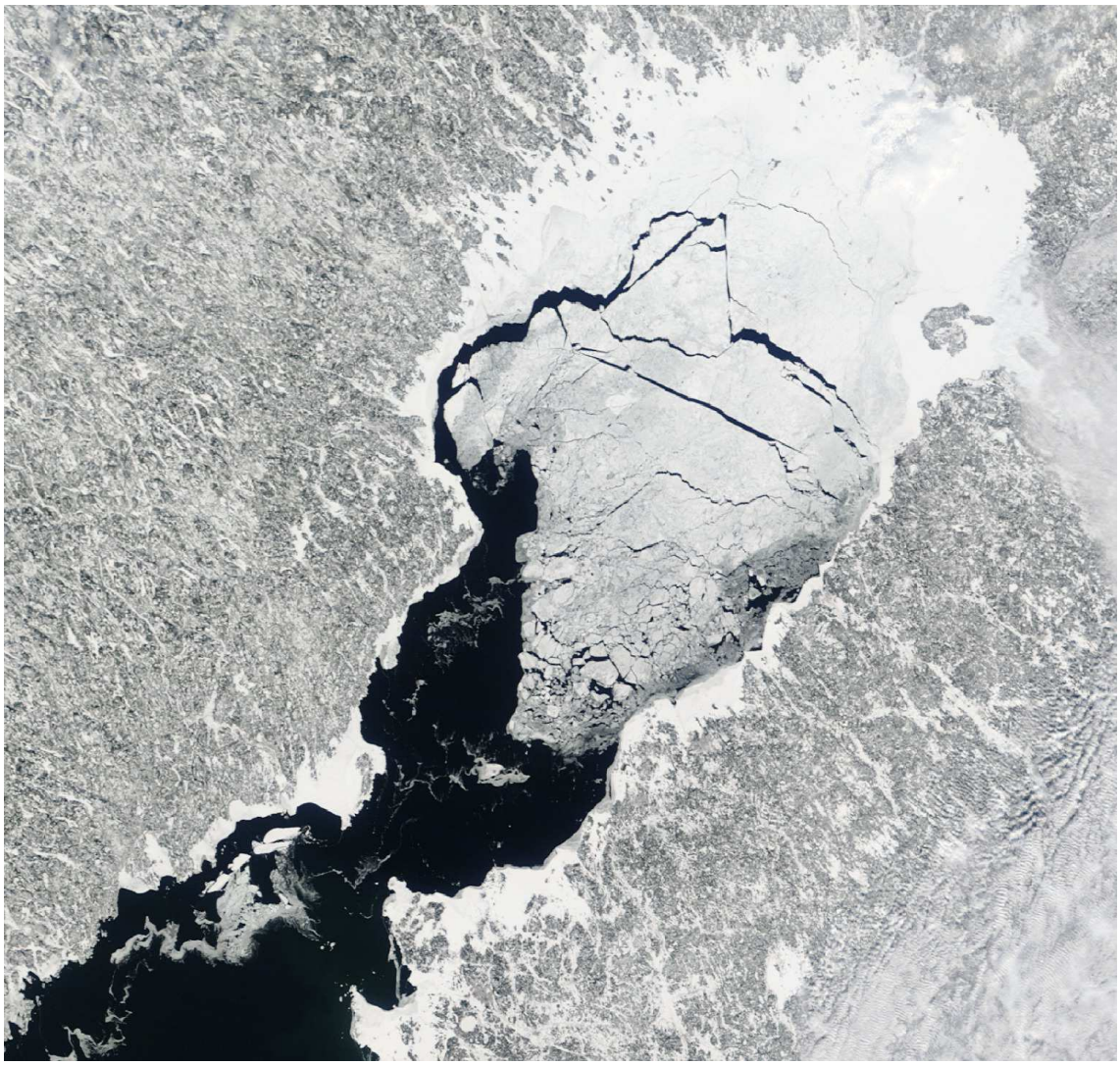

Figure 5.1: True color satellite image of the Bay of Bothnia, 18. March 2009, 10:05 UTC. Image courtesy of NASA.

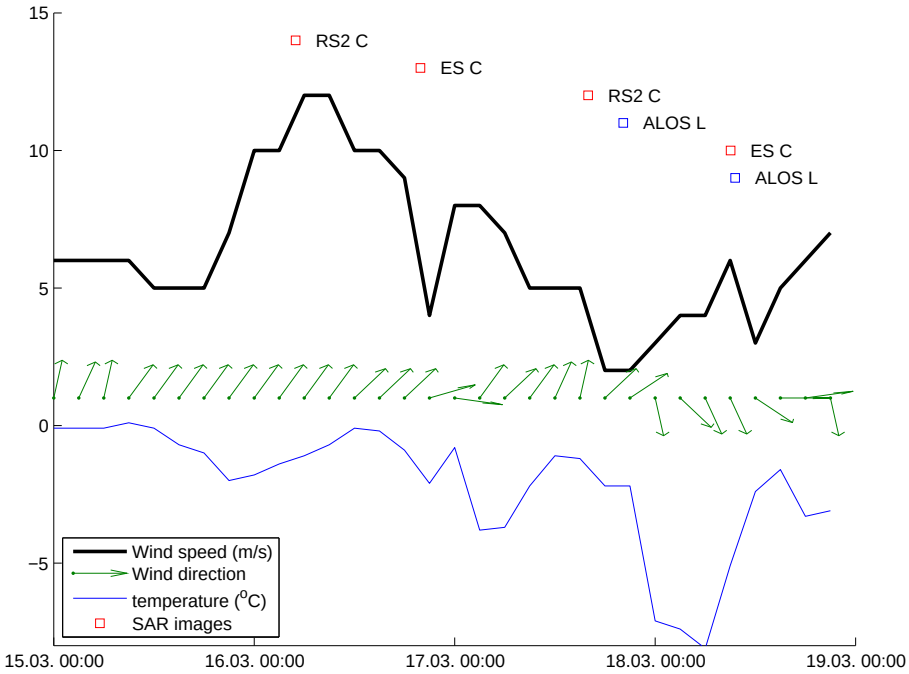

Figure 5.2: Wind and air temperature recorded by the Kemi 1 lighthouse weather station during the experiment period.

5.1.1 Weather and ice conditions during the experiment period

For sea ice, the winter 2008-2009 was milder and shorter than average. This was due to the sea water temperature remaining above average in the autumn and late autumn temperatures staying higher than normal. Freezing commenced in the Bay of Bothnia in latter half of November, but the ice cover extended across the Bay of Bothnia only in the end of January. February was a normal winter month, and the maximum ice cover, 110 000 km^2, was recorded on the 20th day. Much of this ice was thin, and after a cold perioid, warmer southwesterly winds pushed ice northwards during March. On the 16th day only the Bay of Bothnia and northern Gulf of Finland had a significant ice cover. (The Baltic Sea Portal, 2009)

Figure 5.2 summarizes the weather during the experiment, as recorded by a weather station at the Kemi 1 lighthouse. During the acquisition of the first satellite image, strong southwesterly winds were pushing ice towards northeast and the temperature was relatively mild near 0 C. The next two days saw the wind grow more gentle and turn to north.

As can be seen in figure 5.3, most of the drift ice in the Bay of Bothnia is deformed by ridging, and some rafting is also mixed in. Not much level ice remains, the well-defined areas being west of Hailuoto and southwest from Tornio. There is

no new ice to be found, but large sections of landfast ice lie around the coastline. Reported level ice thicknesses are from 10 to 50 cm in the drift ice and up to 70 cm in landfast ice, but six icebreakers are on duty assisting ships.

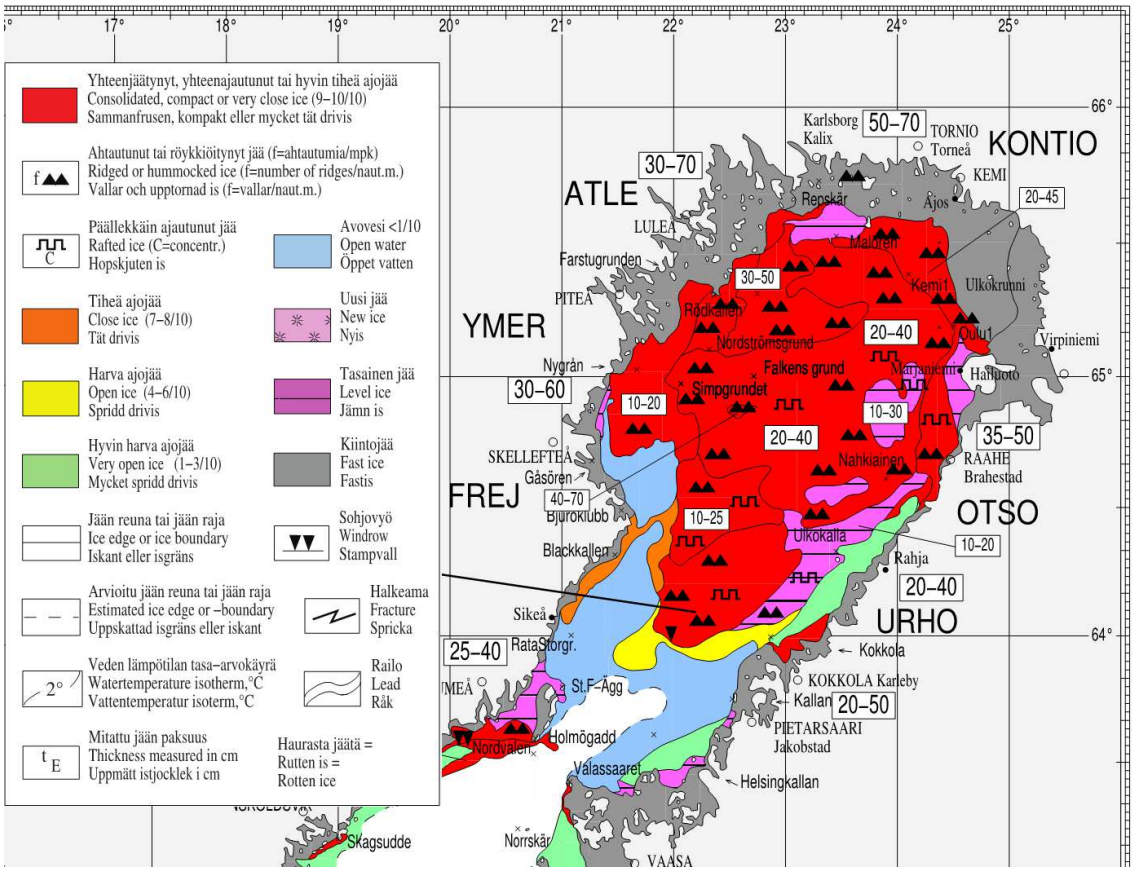

Figure 5.3: Excerpt from an ice chart published on 17. March 2009 by the Finnish Meteorological Institute. Most drift ice is compact and heavily deformed, with some patches of level ice and more open ice.

5.1.2 The satellite image dataset

For this work, six satellite images were chosen for closer inspection. Images 5 and 6 are of different frequency bands and almost simultaneous, with only 32 minutes between them. This is desirable for comparing frequency bands, and a unique occurrence in the set of images that were available. Further, there were relatively many images covering most of the Bay of Bothnia right before this pair.

All images were reprojected to the Mercator projection (using reference latitude 61°40′) and cropped to the area of interest. The image dimensions in pixels were 3900 by 3700, such that each pixel represented an area of 100 x 100 meters, the nominal resolution of the employed RadarSAT 2 capturing mode.

image #	tag	satellite	time (UTC)	t	SAR band
1	R1	RadarSAT	16. 3. 2009 4:59	t_0	C
2	E1	EnviSAT	16. 3. 2009 19:54	t_0+14:55	C
3	R2	RadarSAT	17. 3. 2009 16:00	t_0+35:01	C
4	A1	ALOS	17. 3. 2009 20:12	t_0+39:13	L
5	E2	EnviSAT	18. 3. 2009 9:04	t_0+51:05	C
6	A2	ALOS	18. 3. 2009 9:36	t_0+51:37	L

Table 4: List of satellite images used in this work

5.2 Performance metrics for motion estimation

In an ideal case, the performance of a motion estimation method would be evident. For the remote sensing of sea ice, it is often not possible to set up test cases or record ice movement by other means in the required scale. Historically ice motion vectors have been evaluated by comparing them to expected wind patterns (Ninnis et al., 1986), results of other established motion estimation algorithms (Thomas, 2004) and GPS buyous and numerical model results (Karvonen et al., 2007; Karvonen, 2012). It is also possible to evaluate the performance of an algorithm by its internal variables and the realism or the lack of realism of its output. Performance parameters for a cross-correlation result include the height of the correlation peak, the regression coefficient, and, derived from the correlation result, peak-to-background ratio while the motion estimate can be evaluated against the expectation of uniformity, flagging as errors all vectors that differ significantly from all of their immediate neighbors (Kwok et al., 1990).

For the purposes of this work, comparing the performance of the algorithm for different radar bands, it is not necessary to validate the results against all possible data. The work concentrates on evaluating the cross-correlation results and produced motion fields in the background of the observed wind pattern. Two kinds of results are calculated automatically for each estimated motion field: statistical properties of the ratio of two highest correlation peaks (the higher, the better) and the average difference between a raw motion vector and a median-filtered result vector. It is assumed that the median filtering succeeds at removing spurious values and retains real stepwise changes in the ice motion field, so that the median-filtered motion field represents the real average motion. Even when this is not the case, unrealistic vectors will not match it, so these cases cannot produce false successes.

A motion vector is considered good in a “peak margin” sense if the margin between the two highest cross-correlation peaks is at least 15%, a limit found to be a

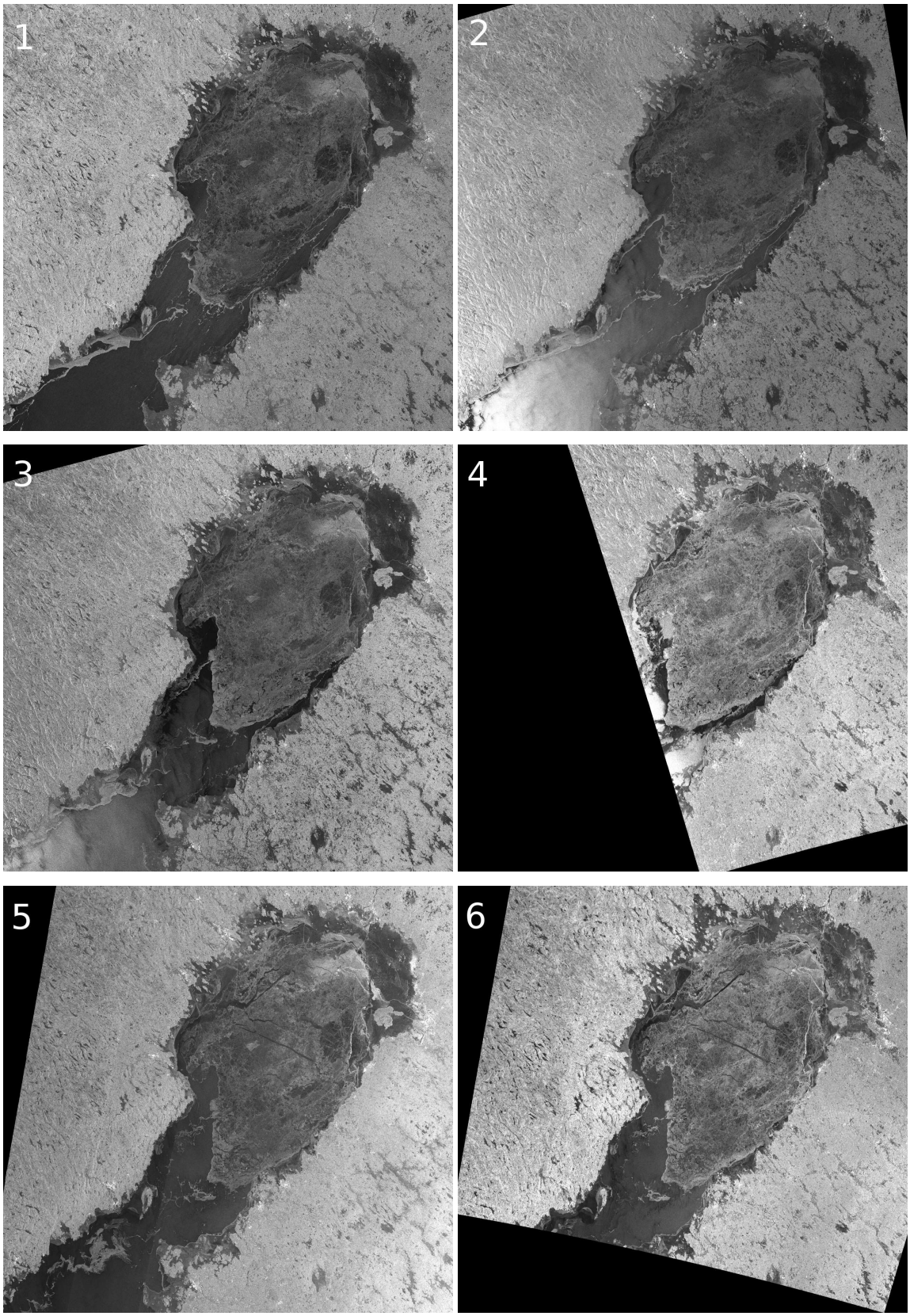

Figure 5.4: (1) 16.3. 4:58 RadarSAT C-band image (2) 16.3. 19:54 EnviSAT C-band (3) 17.3. 15:59 RadarSAT C-band (4) 17.3. 20:12 ALOS L-band (5) 18.3. 9:03 EnviSAT C-band (6) 18.3. 9:35 ALOS L-band

safe margin in this work. A motion vector is considered good in a "regularity" sense if it differs from the median-filtered value by less than 500 meters.

5.3 The motion estimation approach

For this project, a straightforward block cross-correlation program was written in the general purpose C++ programming language. The code works directly in the spatial domain, to allow more flexibility in fine-tuning the computational parameters (Emery et al., 1991) and to allow easy parallelization. Critical parts of the algorithm were programmed in OpenCL C in order to offload the most demanding work to GPU calculation units. OpenCL is a portable language for writing code that can be run in a parallel fashion on a variety of devices. This GPGPU approach provided significant speedups and cut down the calculation time by some orders of magnitude. The OpenCL cross-correlation program can process one pair of images in roughly 20 seconds, as opposed to 20 minutes for a single-core program running on the CPU.

In order to optimize the execution time, the size of the search domain was limited to a $96x96$ pixel window as the amount of fast local memory is 48 kB on the nVidia GPUs that were used. Compared to previous methods, this size is not small, but it limits the maximum displacement to 4.8 km which is too little to catch most ice motion cases. Thus, a multi-step approach was necessary. First, motion would be calculated in a coarse resolution (1/8 of the original or 800 m / pixel, which allows almost 40 km displacements), and median-filtered result vectors would be used as initial guesses for the high-resolution matching step. Finally, the high-resolution result is median-filtered to remove problematic values. For this work, the median filtering radius was chosen to be 3 (as in Karvonen et al., 2007).

For the image windows that were cross-correlated with the search domain, $16x16$ pixel size was chosen. There is a tradeoff involved in choosing this window size, as it has to be large enough to contain a discernible pattern, and at the same time small enough to retain its structure in the time interval separating the pair of images. The chosen size is at the small end of practical options. It was chosen to minimize errors due to deformations, and maximize errors due to lack of discernible patterns within these windows. This way the error fractions are maximally useful for comparing C-band images to L-band images.

The method consists of the following steps:

1. reprojecting and cropping satellite images using the GDAL toolset

2. loading the GeoTIFF images, translating 16-bit greyscale values to floating-

point numbers

3. generating a resolution pyramid for both images, using a 2-d low-pass filter and decimating for every level

4. running cross-correlation for coarse resolution image windows

5. median-filtering the coarse result to produce the average motion field and first guess for next step

6. running cross-correlation for the finest resolution image windows

7. saving this result and a median-filtered version (radius 3) of it in an ASCII text file.

The results were analyzed and plotted using the Matlab and Octave programs and the M_Map mapping package which is freely available online.

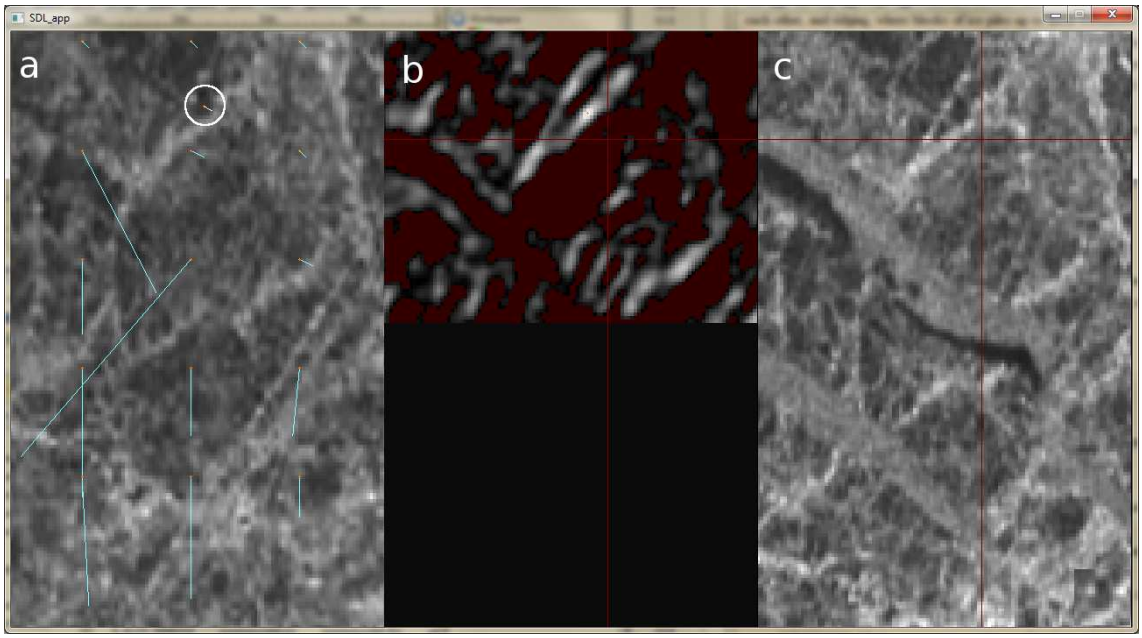

Figure 5.5: Screenshot of the motion estimation program written for this work. a) zoom-in of the first image with some detected motion vectors. b) the cross-correlation result for the circled vector. Red represents negative c-c. c) aligned zoom-in of the second image of the pair. Notice the newly formed NW-SE aligned lead.

5.4 Satellite image processing

Algorithms used for operational satellite image analysis are often tuned to the specific instruments. As the objective of this study is to compare different instruments, no instrument-specific tuning was done. The images still need georectification, and typically a landmask is used.

5.4.1 Projections and coordinate system corrections

Satellite radar images are rectangular datasets, and straightforward rendering on a computer screen maps recorded intensity values on a plane. The real, significantly curved surface is distorted already by the imaging geometry. The orientation of the recorded rectangle also varies, one axis being aligned with the satellite's orbit. Thus, the images must be projected onto a standard projection before they can be processed further. This projection is achieved by utilizing tie points that are provided with the image. These tie points map certain pixel locations of the image to fixed coordinates in latitude and longitude, using the WGS84 datum. Usually there is still slight error after this projection step, which must be corrected by matching immobile features between the images. If tie points are not available, it would be possible to generate them by locating features of known location from the images. Possible features include man-made structures like cities and natural patterns like coastlines, small islands and the like. For every pixel in the target image, an intensity value is interpolated from the source image using this mapping.

For this work, SAR images are rectified to the Mercator projection with a reference latitude of $61^{\circ}40'$. This rectification was chosen, as it matches the projection used in both the Baltic Sea nautical charts for this area, and previous ice motion estimation work on the Baltic (Karvonen, 2012).

5.4.2 Masking land points

For sea ice motion estimation in the narrow basins of the Baltic Sea, it is essential to differentiate between land and ocean as most satellite images of the area will contain both. Land masking could be done by a vector dataset of shorelines, such as the GSHHG by NOAA (Wessel and Smith, 1996), or a gridded topography. For this work, it was convenient to use topographical data produced in the The Leibniz Institute for Baltic Sea Research. This data covers the whole Baltic Sea area in a grid of 1 nautical mile spacing, providing a representative average of the water depth and the land height and proposed landmasks for both points of view (Seifert

et al., 2001).

This topography data was acquired in the NetCDF format and converted to GeoTIFF. As a georeferenced image, the topography could be handled by all the same tools as satellite images; resampled to any desired projection and cropped to any size that might match the variable extent of satellite images. Further, numerical depth data allows the final mask to be fine-tuned and landfast ice, generally found where the depth is less than 10 meters, could be treated separately.

The masking of one or both satellite images, by setting land pixels to black, was attempted, but it was deemed better to run the motion detection with unmasked images. Masking is done just before the analysis step. This allows separate analysis for land and sea vectors. As a drawback, image windows that include the coastline possibly generate two valid cross-correlation peaks. After acquiring the finest resolution motion estimates, the median-filtered values for land points were further interpolated across the sea area, to produce a seamless estimate for the image registration error. This registration error was finally substracted from the motion results recorded for the drift ice.

5.4.3 Possible improvements

Raw satellite images have varying illumination in different parts of the image. This is due to the variation in incidence angle, apparent in 5.4b and 5.4d. The illumination could be corrected prior to the motion estimation step, and it could only improve the results. However, as this work uses normalized cross-correlation of small windows, and the variation in incidence angle in each image window is small, a linear correction would not significantly improve the matching capability.

Speckle noise is a characteristic granular degradation in radar images. In SAR images, specle noise is multiplicative and statistically independent of the signal (Tso and Mather, 2009). Many filters have been developed for speckle filtering, from straightforward mean- and median-filter methods to adaptive filters.

For future development, if the algorithm written for this work is to be used operationally, to calculate the best possible motion estimates, speckle filtering should be applied. As edge detection is often done in sea ice motion estimation, future experiments should include some form of it. Both of the above image processing steps should be calibrated to provide the best possible results, especially for the mixed band image pairs, work that the fast GPGPU implementation makes feasible to do even for large datasets. Additionally, the algorithm should use overlapping image windows for better chances of catching good, whole features in them.

6 Results and discussion

As images 5 and 6 (see table 4 and figure 5.4) are separated by only 32 minutes, they are assumed to represent the same ice situation in C- and L-bands, respectively. This means that the motion estimate between any image and either one of this pair should be equivalent, save only for the differences caused by image properties. Such parallel motion estimates were used to quantify these differences, first by evaluating the resulting motion vectors, then by looking into statistical properties of the results, and finally by analyzing the geographical distribution of errors.

6.1 Visual comparison between L- and C-band images

The almost contemporaneous images (e) and (f) in figure 5.4 show the same general picture of the ice pack. No ice-related change can be distinguished visually, so all differences are taken to result from differences between the imaging instruments. As a general difference, the L-band image (f) has more contrast within the sea area. The coastline is also more easy to distinguish, while in the C-band image, the coastline disappears in some, especially northern, locations. Below, specific differences in these two images are evaluated in detail.

To summarize, ice types in the drift ice region appear similarly in images of both frequency bands. Sometimes the C-band image is better at distinguishing the edge of an ice floe, and sometimes L-band shows features not visible in the C-band image (see east edge of figure 6.5), but for most features, the L-band image simply seems to provide stronger contrast. On the other hand, many features in landfast ice appear differently in C- and L-band images. Perhaps a long, relatively peaceful evolution of an ice surface produces surface roughness in length scales comparable to the radar wavelengths.

6.1.1 Landfast ice

Any features in landfast ice are either thermodynamic or old, because, by definition, landfast ice is immobile and non-dynamic. Very near the coast, the initial thin ice can survive without disturbances, but within the archipelago, the thin ice possibly moved and deformed before becoming fixed. As can be seen in figure 6.1, the archipelago looks more homogenous and dark in the L-band image. Conversely, the C-band image shows a large hazy feature, conspicuously framed by the shipping lanes.

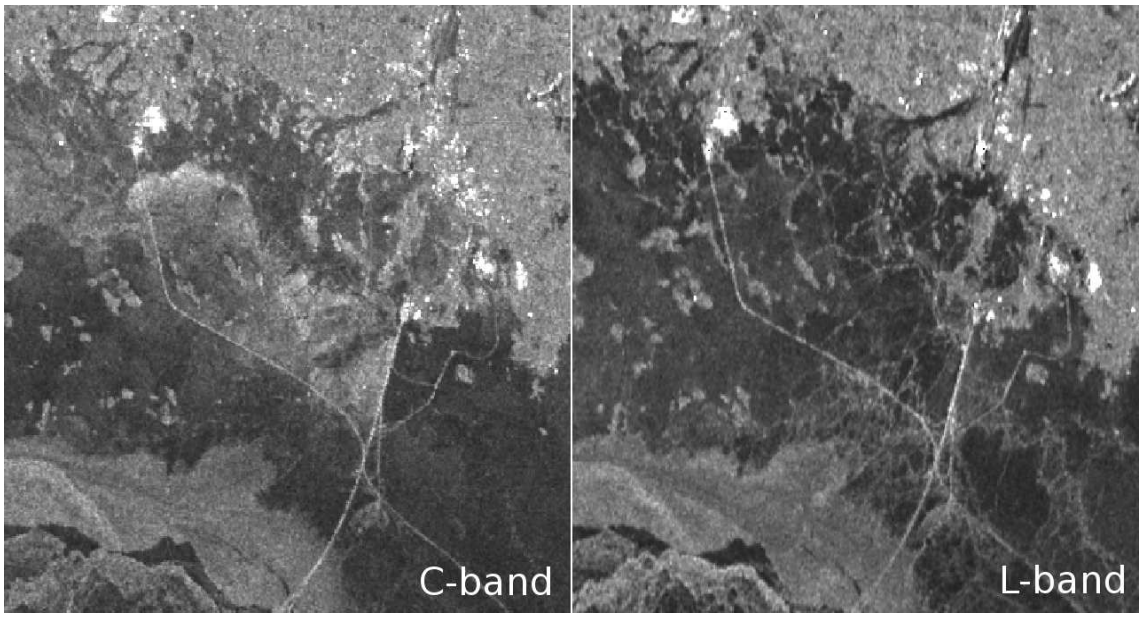

Figure 6.1: Detail of landfast ice in northern Bay of Bothnia on 18. March 2009. White tracks are shipping lanes to Tornio and Kemi, which appear very bright in SAR images.

The linear or web-like features visible in the L-band image but missing from the C-band image are probably remnants of small ridges within the ice volume, hidden beneath a relatively smooth surface. These could be visible through L-band's greater volume scattering. The surface could be smoothed by repeated melting and refreezing of ice and overlying snow cover.

Features missing from L-band image but visible on the C-band image, on the other hand, are probably caused by surface roughness smaller than the L-band wavelength (12 cm). The shipping lanes that constrict the bright haze in the C-band image, provide a hint of its formation. This was possibly mobile broken slush, which froze to form a rough surface on the nothern side of the shipping lanes.

Near the southwest corner, there's a brighter gray band without clear features. This is the shear zone at the landfast ice boundary, experiencing deformation by external forces but still attached to the landfast ice, islands, or the shallow sea floor. The dark feature under it is open water or thin ice in a lead, and we also see some drift ice in the corner of the image. These features look similar in both images.

In figure 6.2, the L-band image has ill-defined bright features in the landfast ice zone while the C-band shows little scattering. To know the evolutionary history of these features, one would need to track their formation from the beginning of the freezing period. Here, too, early-season deformations could be masked by smoothing

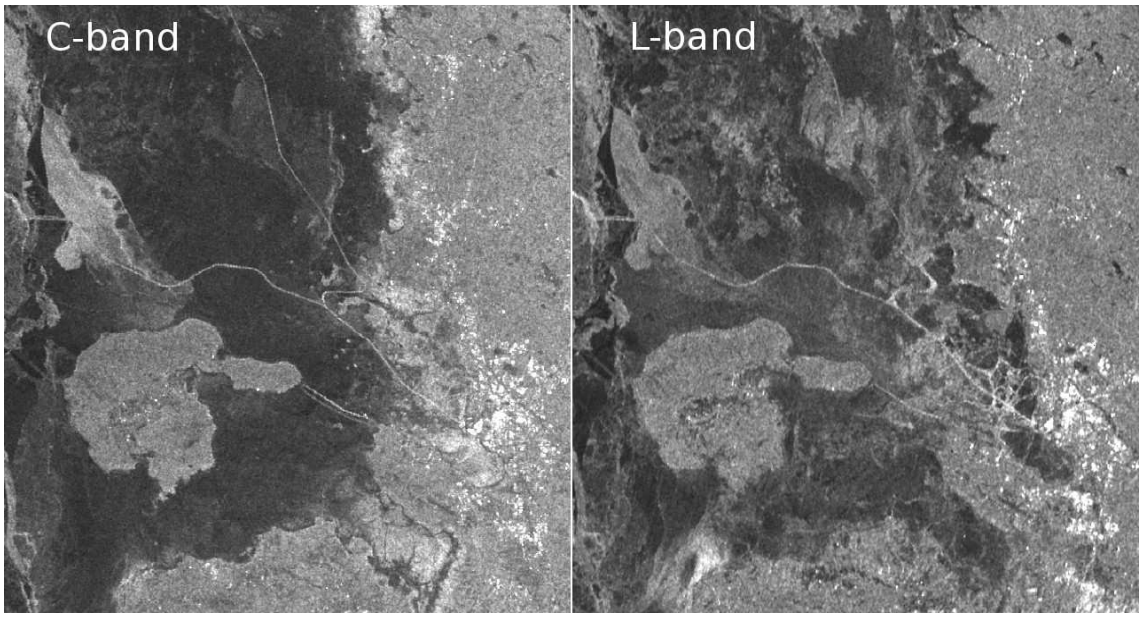

Figure 6.2: Detail of landfast ice in northern Bay of Bothnia around Hailuoto, offshore from Oulu, on 18. March 2009.

surface processes. The bright feature north of Hailuoto island, which appears similar in both images, is probably a field of broken ice, often called a rubble field, analogous to a very wide pressure ridge.

Comparing these images, it can be concluded that landfast ice can be a tricky substance for matching windows of SAR images of different bands. Some features will appear similar but at different intensities, and some areas will look completely different.

6.1.2 Level ice

Some ice classified as level ice can be seen in the southwest corner of figure 6.2, southwest from Tornio in figure 5.4, and in the dark ovals in figure 6.3. These areas show up as relatively dark areas, presumably because of relatively low specular reflection, in SAR images of both wavelengths. In general, C-band shows these features darker than L-band, as L-band will cause more volume scattering from beneath the level surface. In some areas level ice is relatively featureless and in others rather detailed. Some of the areas look identical in C- and L-bands, others show more contrast in L-band. However, based on visual inspection, correlating image windows in level ice seems feasible. This analysis is limited by the small amount of level ice.

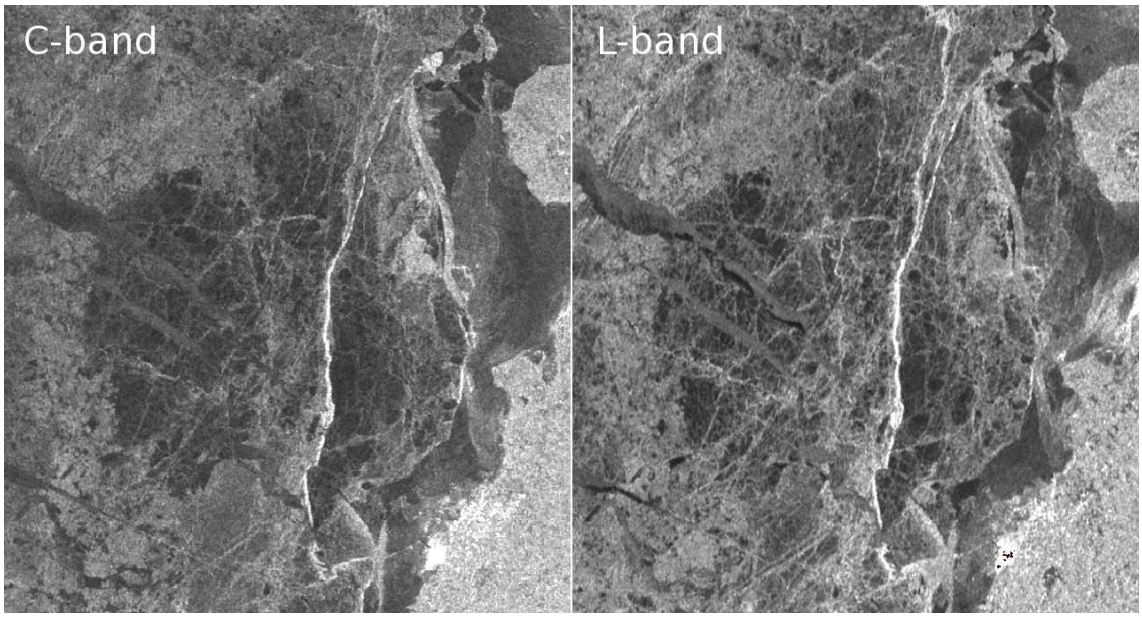

Figure 6.3: Circular dark area classified as level ice near Raahe on 18. March 2009.

6.1.3 Open ice

Sea areas with less than 60% ice cover are classified as open ice. In open ice, separate ice floes drift freely among waves. Using both frequency bands, ice forms similar gray curls, visible in figure 6.4, that should allow motion detection using cross-correlation to work well. Most notable visible differences are dark lines in the open water in the L-band image, and slightly better contrast in the C-band image. However, these formations appear fragile and susceptible for changes, which makes tracking them rather demanding.

6.1.4 Compact drift ice

Drift ice, classified in finnish ice maps as consolidated, compact or very close ice, often covers the central Bay of Bothnia during winters. It is a mobile continuum, it deforms readily, and transmits compressive forces over large distances.

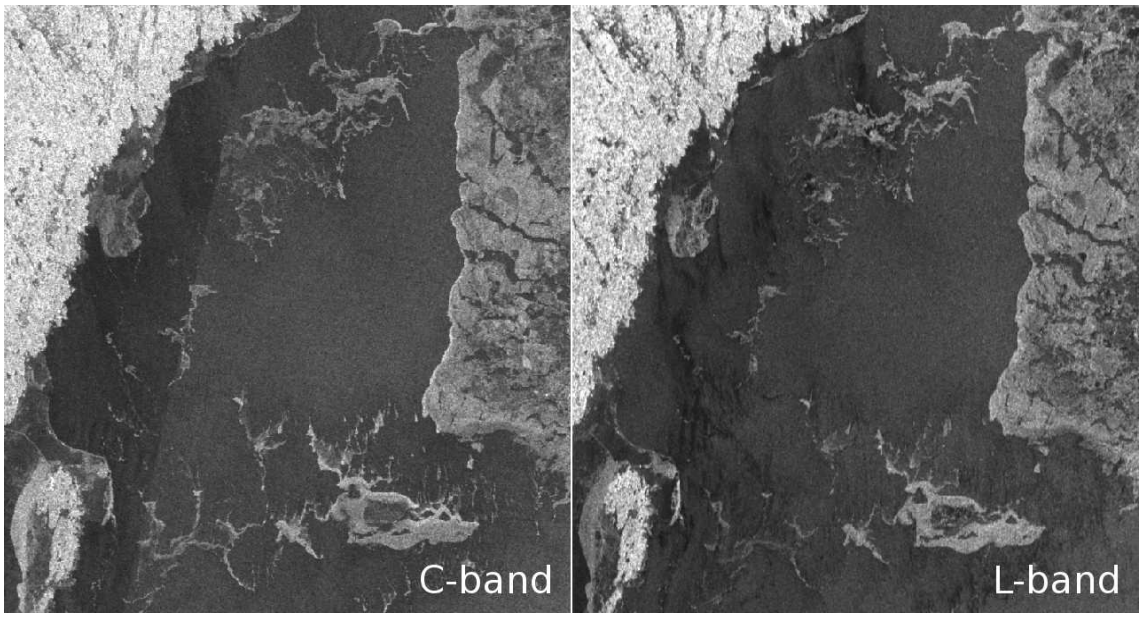

Figure 6.4: Open ice between the Swedish coast and the compact ice pack in North Kvarken on 18. March 2009.

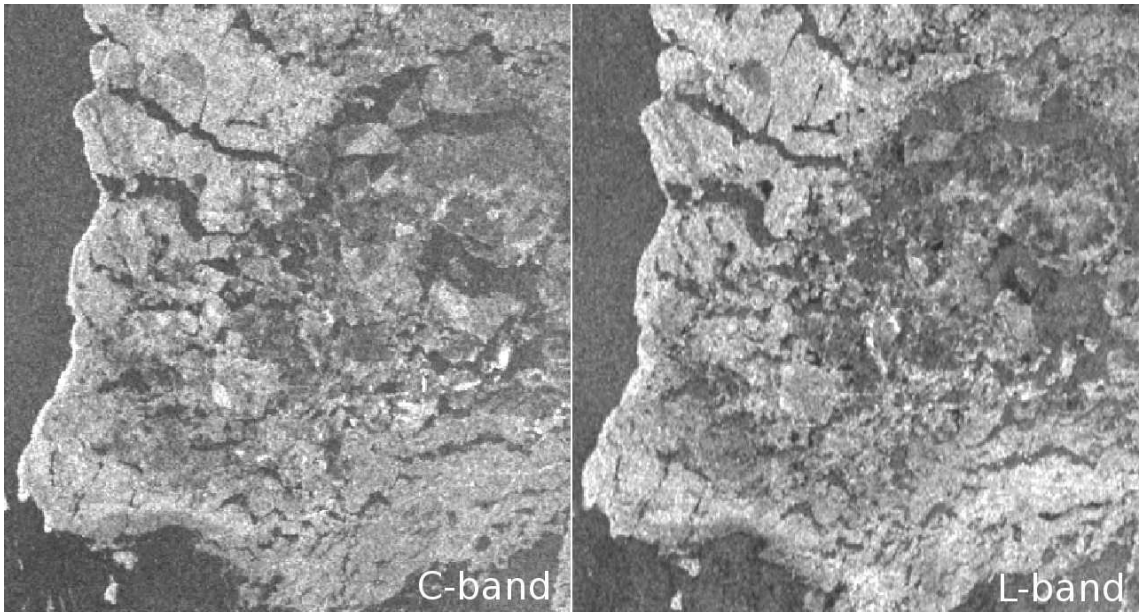

Figure 6.5: Southern tip of the compact drift ice on the Bay of Bothnia on the 18. March 2009.

In figure 6.5, separate but closely packed floes of compact drift ice can be seen, sometimes separated by leads or other open water features. Many distinct ice floes are recognizable in both images, but the fainter floes near the east edge are not visible in the L-band image despite standing out very clearly in the true-color image

5.1. The L-band image seems less able to distinguish the border between a lead and a smooth ice floe, and occasionally there is texture not present in the C-band image, like the bright features in the southeast corner. However, the edge of open water is well visible and similar on both frequency bands, and most ice floes seem similar enough for motion estimation.

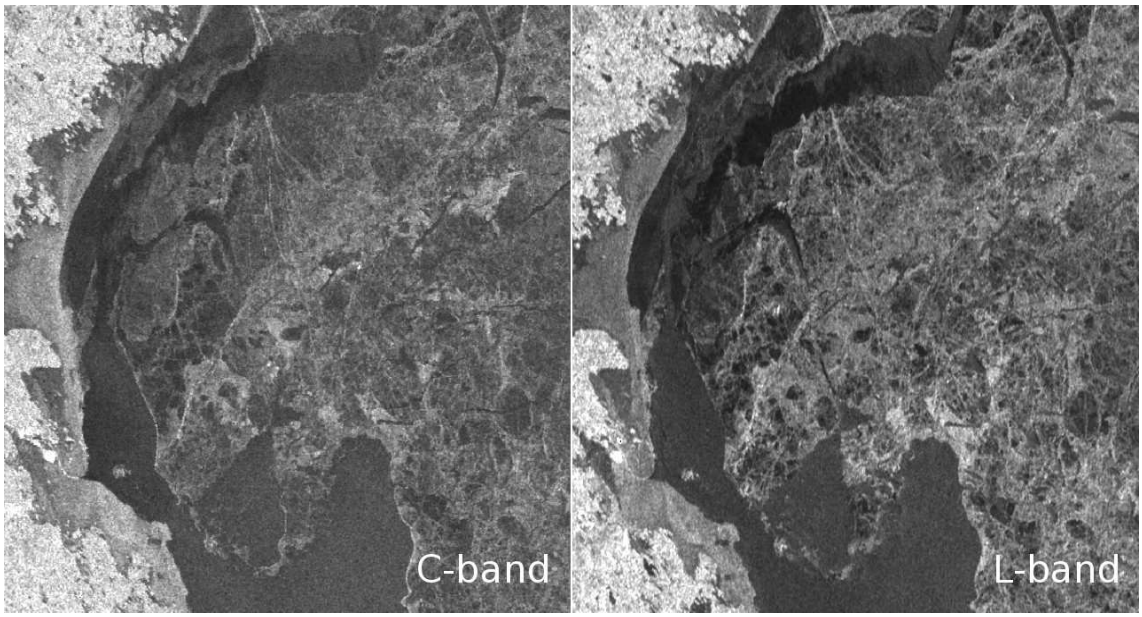

Figure 6.6: Drift ice on the western Bay of Bothnia, 18. March 2009.

In figure 6.6, a compact and mostly continuous ice pack is seen in both C- and L-band. The texture is similar, and the images don't reveal significant differences in ability, but L-band SAR produces significantly better contrast.

It is evident from figures 6.6 and 6.7 that sometimes leads appear very dark in L-band images. In general however, leads are visible in both kinds of images, and should pose no special problem for motion estimation in a mixed-frequency image pair.

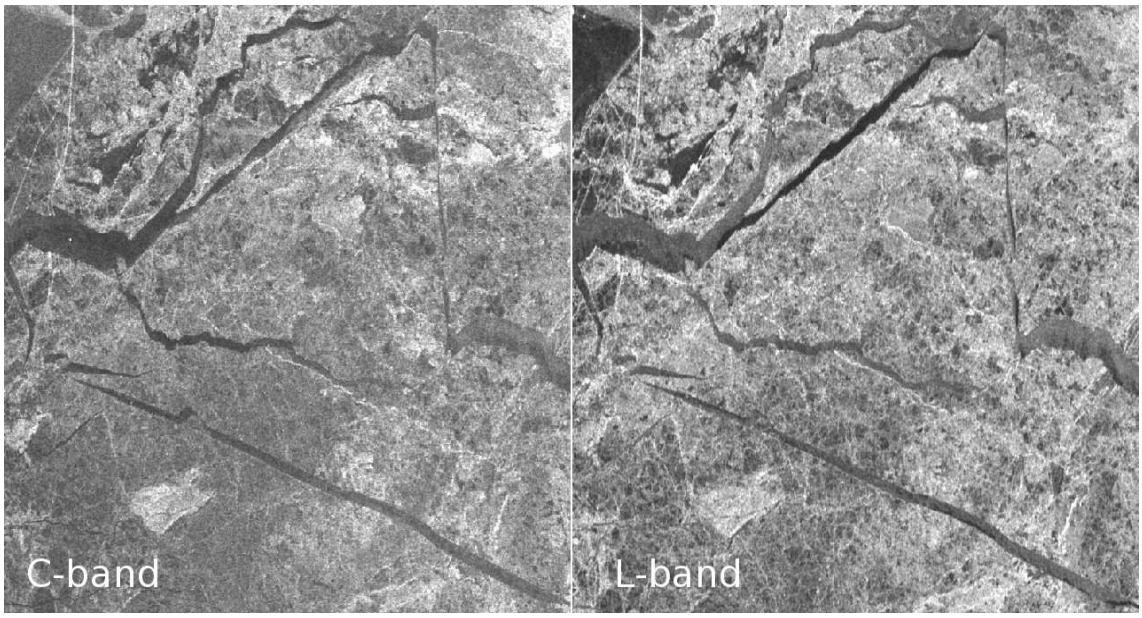

Figure 6.7: Leads in drift ice, Bay of Bothnia, 18. March 2009.

6.2 Motion estimates

To summarize, the motion estimates calculated for image pairs covering the same time interval are similar in all cases. For a C-C or L-L band image pair, the matching is better and motion results may be found for a larger area than in a mixed pair. Based on the metrics defined in chapter 5.2, an L-L image pair is superior for motion estimates compared to C-C pairs, while mixed pairs are still feasible despite them presenting the most problematic case.

The average motion for the whole experiment period is shown in figure 6.8. Both a C-C pair and a mixed L-C pair do a good job for most of the drift ice. The motion fields are almost identical, and the average eastward motion is well supported by the southwesterly winds that turned north towards the end of the period. It is notable though, that neither image pair produces motion for the southern tip of the drift ice area. These two parallel estimates correspond to the first row of table 5.2.

In figure 6.9, we see an average southward movement for the latter 36 hours of the experiment. This is in line with the prevailing winds as well, as the northward transport of ice had stopped before the winds turned north. This time, for the C-band pair, also the southern ice edge is successful but 6.9a shows no motion where 6.9b finds realistic vectors. These two parallel estimates correspond to the second row of table 5.2.

The four latter motion estimates, represented on the two bottom rows of table

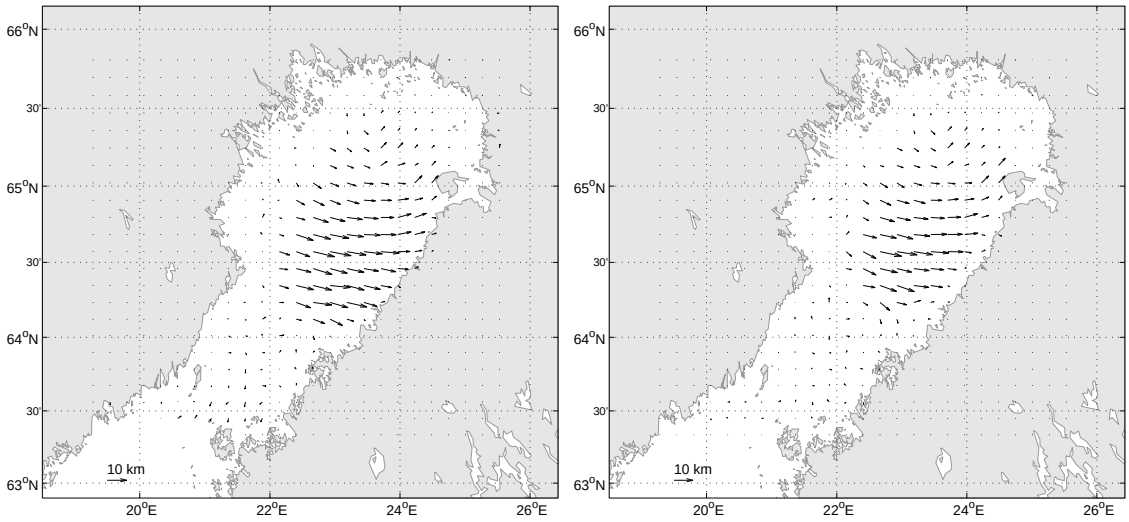

Figure 6.8: a) motion vectors from image pair 1&6, of C- and L-band, respectively. b) motion vectors from image pair 1&5, both C-band.

5.2, appear very much like 6.9b. This is because each of these image pairs cover the whole period of northerly winds.

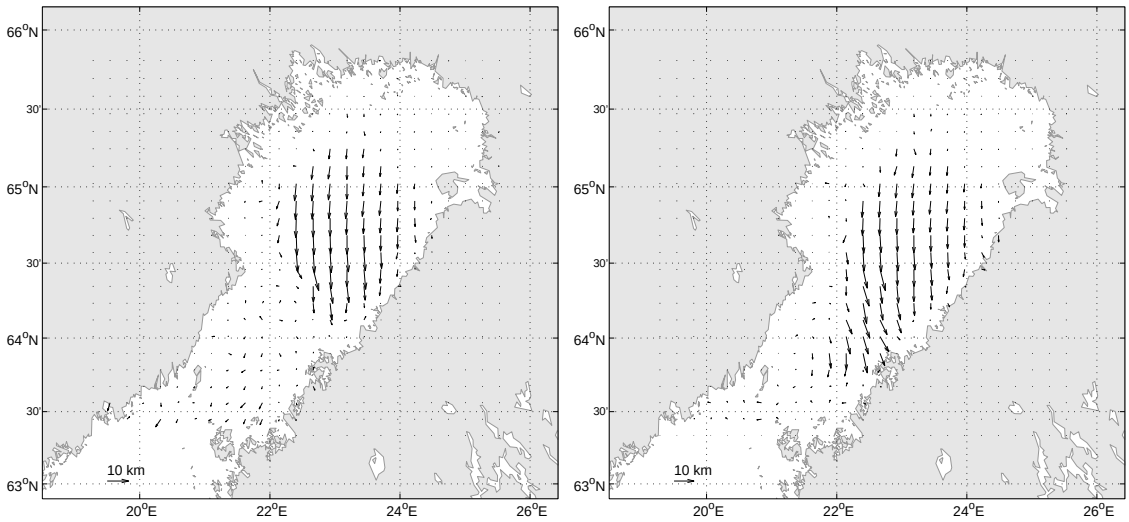

Figure 6.9: a) motion vectors from image pair 2&6, of C- and L-band, respectively. b) motion vectors from image pair 2&5, both C-band.

Comparing the performance of parallel image pairs, some observations were made. As expected, the motion estimation algorithm works better for shorter timescales, as less deformation has had time to happen. For all image pairs, large-scale motion estimation was successful. All motion estimates contained a large number of spurious vectors too, but a radius 3 median filtering was found to produce a realistic and smooth motion field. Thanks to the median filtering, the algorithm

works even if only 13 % of motion vectors are correct. This success rate is thus found sufficient for detecting the large-scale motion. However, as evident in figure 6.9, a mixed image pair can fail in details in some sub-regions.

image pair	pm-good	reg-good	image pair	pm-good	reg-good
R1-A2 (CL)	17.6 %	14.0 %	R1-E2 (CC)	19.6 %	16.2 %
E1-A2 (CL)	20.1 %	14.2 %	E1-E2 (CC)	22.7 %	16.7 %
R2-A2 (CL)	24.7 %	15.8 %	R2-E2 (CC)	27.9 %	18.6 %
A1-A2 (LL)	45.6 %	28.4 %	A1-E2 (LC)	30.7 %	18.7 %

Table 5: Performance values for parallel image pairs, as the percentage of displacement vectors that are accepted as "good" based on the peak margin- and regularity -criteria defined in 5.2.

Homogenous image pairs are found better than mixed pairs. Further, the L-band is found more suitable for motion estimation in this data set than C-band. Unfortunately, it seems that a large peak margin in cross-correlation is not sufficient as an indicator of correctness. In closer investigations it was found that a motion estimate using the highest peak is often correct even if the second-highest peak is just barely lower.

6.3 Validation of motion estimates

For the experiment period, no in-situ ice motion observations exist. There were no drifter buoys at sea, and operational motion estimation using C-band images was not done during that period. As requested, Juha Karvonen produced motion estimates using the same images and his own algorithm. No ice type classification masks or other supporting data were available, so these motion estimates are not ideal for comparison and do not represent the quality in operational runs.

As seen in figure 6.10, both algorithms produce the same large-scale southward movement successfully. Details differ, though. The algorithm written for this work produces a continuous motion field for the drift ice area, while the reference algorithm result has detail that is not reproduced in the new algorithm. Some of this detail is spurious vectors from the open water area, which would evidently be removed by an ice type classification mask.

It is concluded that the algorithm written for this work can produce real, reproducable motion results for the Bay of Bothnia.

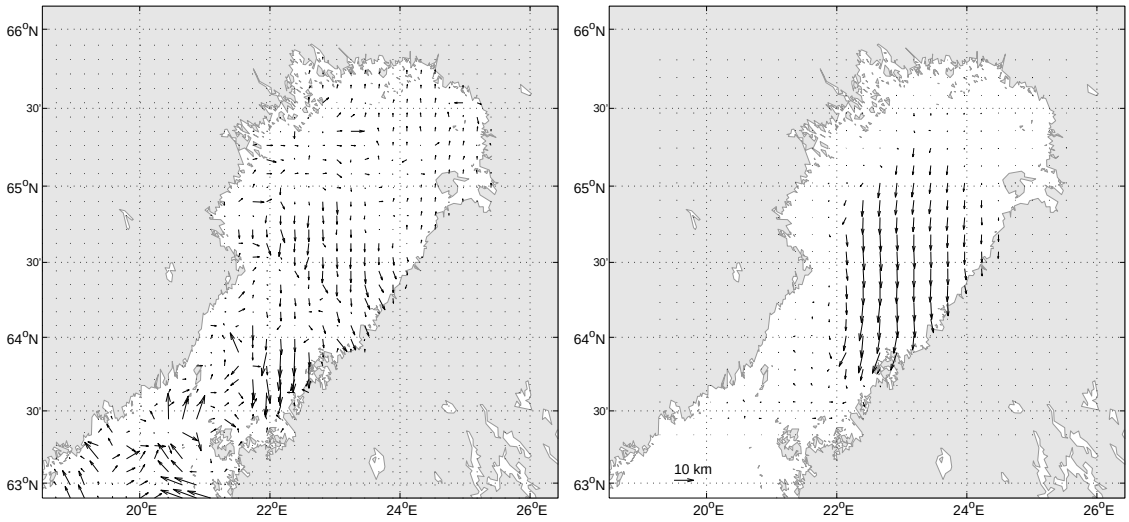

Figure 6.10: Comparing algorithms for ice motion by image pair R2-E2. a) Motion estimation by Juha Karvonen's algorithm. b) Similar result produced by the algorithm developed for this work.

6.4 Statistical performance of image pairs

Overall, both C- and L-band image pairs and mixed image pairs show similar statistical properties in the motion results. The maximal normalized cross-correlation coefficient found (ρ in equation 3.4) is mostly between 0.2 and 0.6, with some matches reaching up to 0.95. As can be seen in figure 6.11, for C-band pairs the worst match is around 0.2. This is closer to 0.4 in the L-band pair of figure 6.12, which has overall higher correlation coefficients.

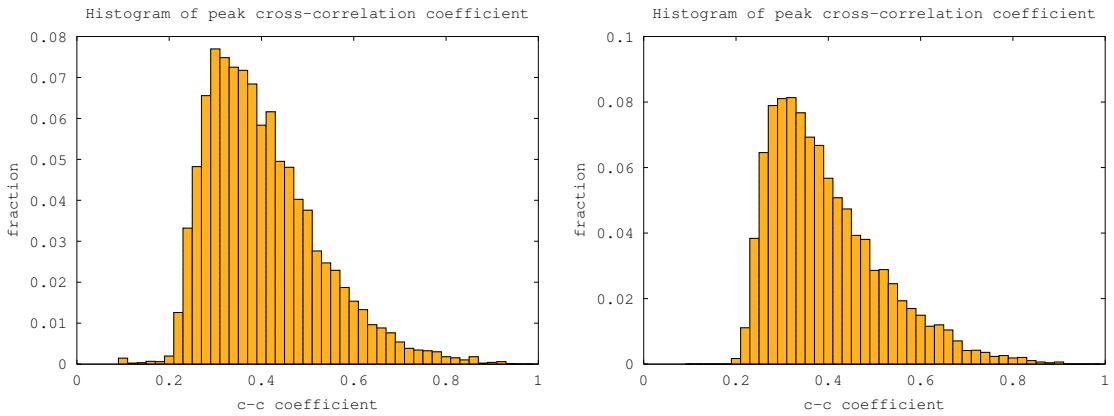

Figure 6.11: Maximum cross-correlation for matched windows in the R2-A2 image pair (CL, left) and the R2-E2 image pair (CC, right)

The ice conditions and their change are the most important factors of success.

This is evident from 6.12b. The A1-E2 image pair boasts large c-c coefficients despite mixing two different wavelengths.

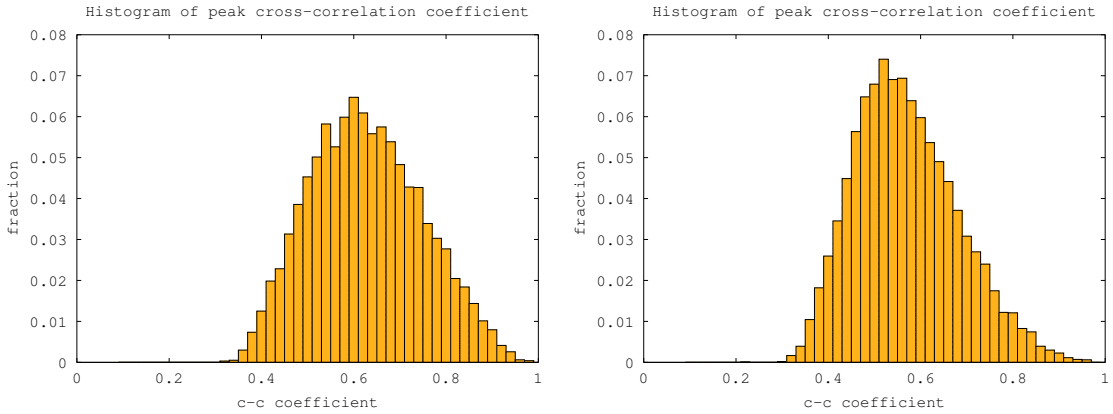

Figure 6.12: Maximum cross-correlation coefficient histogram for the A1-A2 image pair (LL), left, and the A1-E2 image pair (LC), right.

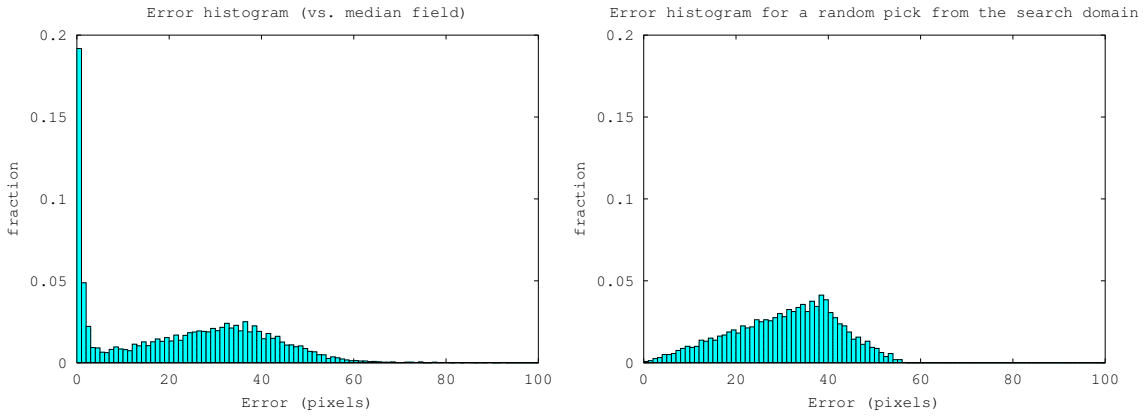

Figure 6.13: a) Histogram of motion estimation error in the R2-E2 image pair (CC, right), and b) error histogram corresponding to a random pick.

The histograms for motion estimation error magnitude are all rather similar. An example is shown in figure 6.13a. The histograms of error show a strong peak for no or very small error and a distribution characteristic to this problem. This distribution roughly corresponds to the idealized theoretical distribution of the distance of a random point, shown in figure 6.13b. This distribution arises from the fact that the search window is square and it allows at most 40 pixels of displacement in each dimension. It is concluded, that there are no systematic errors in the motion estimation algorithm, but otherwise this approach is not useful.

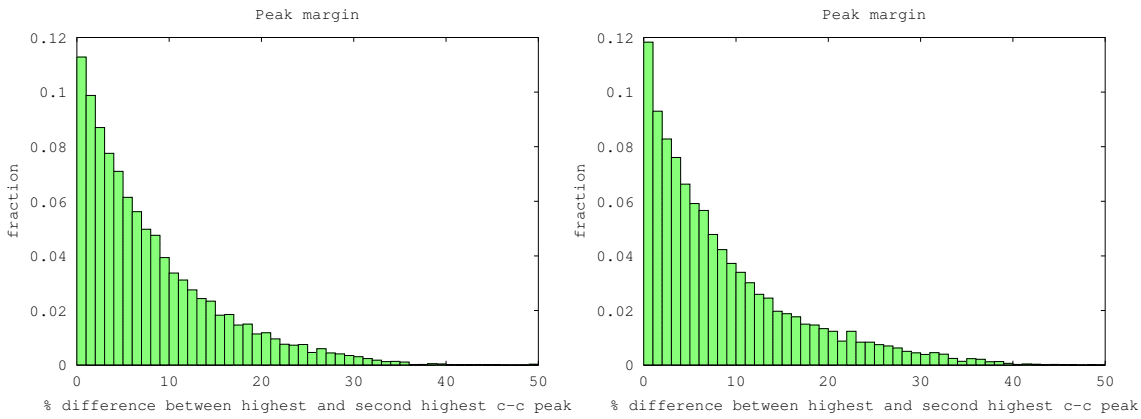

Figure 6.14: Difference in percent between the highest and second-highest cross-correlation peak in the R2-A2 image pair (CL, left) and the R2-E2 image pair (CC, right)

Considering the margin between the two highest correlation peaks, in figure 6.14 it can be seen that a CC pair is better than a mixed CL pair at finding unique peaks. The difference is small though, and very often the highest peak stands only slightly above the second contender. It was expected that the MCC method is weak in producing unique cross-correlation peaks, but these histograms provide a good reason for improving the situation somehow. In the very least, the algorithm could consider N highest peaks for the median filtering steps.

6.5 Geographical distribution of errors

The geographical distribution of errors was calculated for the test cases with smallest time difference in order to evaluate problems stemming from local effects and not changes that occur over longer time intervals. Figures 6.15a and 6.15b correspond to the same time interval, and show that a C-C pair is stronger than a C-L pair in all localities, but the mixed-band pair also succeeds to some extent everywhere the C-C pair does. Figures 6.15c and 6.15d correspond to another time interval and shows that an L-L pair is much better than a mixed pair, again without any clear difference in the areas of successful motion estimation.

To summarize, all image combinations have troubles with the northwesterly lead opening near the northeast edge of fast ice, and all combinations behave better in the central ice pack. It is clear that a single-frequency pair is desirable, but also that for most regions, a mixed-frequency pair performs reasonably well. No image pair finds more than an occasional good motion vector in open ice of less than 30% coverage. As a slightly surprising find, it seems that the C-band is better for matching image

patterns on land. While this is of no concern for perfectly georeferenced images, this might mean that georectifying LL image pairs might be more problematic.

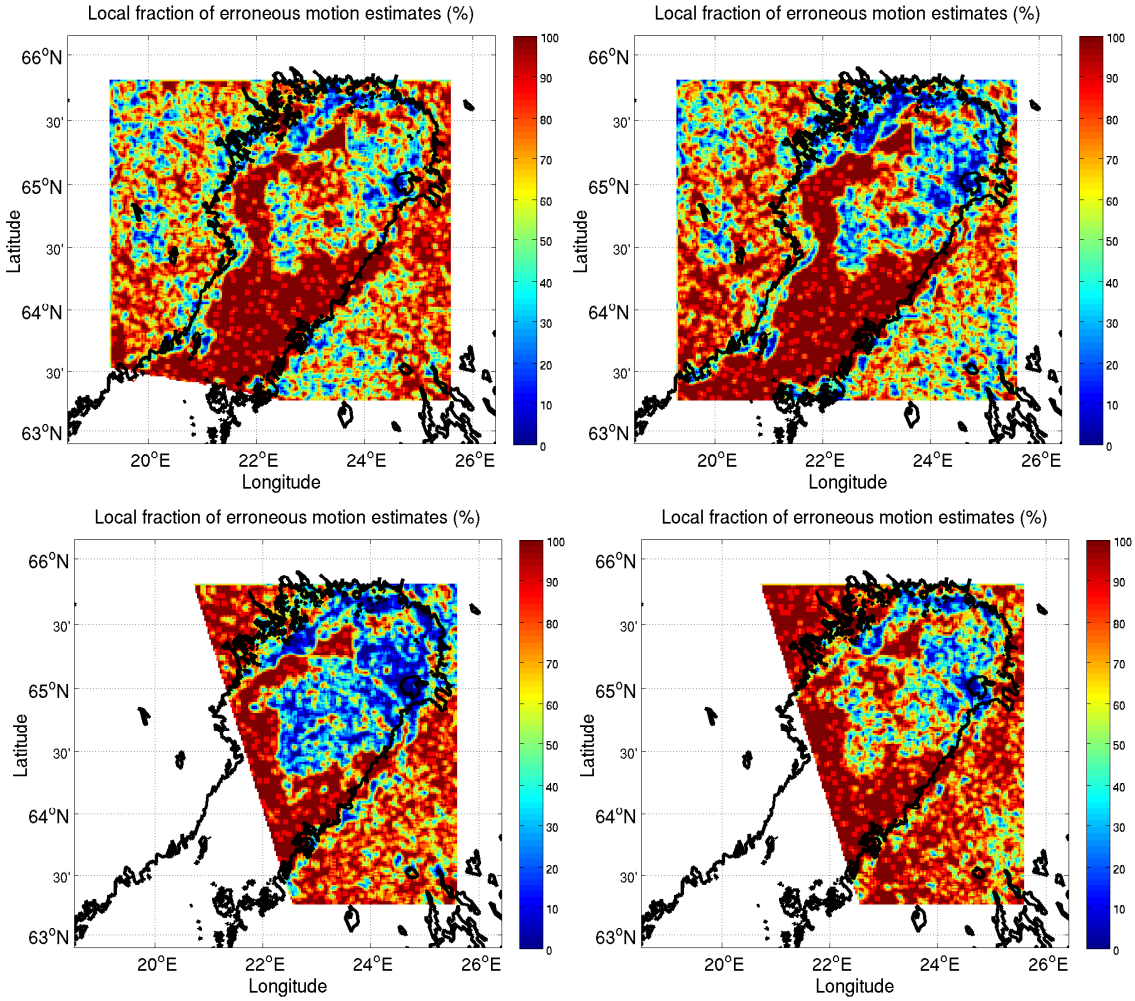

Figure 6.15: Geographical distributions of errors, (a) pair R2-A2 (CL), (b) R2-E2 (CC), (c) A1-A2 (LL) and (d) A1-E2 (LC)

7 Conclusion

It is possible to calculate ice motion using an L-band SAR image together with a C-band image. The program written for this purpose works and produces convincing results, so the chosen algorithm of maximal cross-correlation suits this purpose.

It is clear that L-band images are fundamentally different than C-band images as the ratio of surface and volume scattering is different and some C-band scatterers are invisible to L-band radar. This difference manifests itself primarily in landfast ice, possibly because long periods of thermodynamical changes creates different surface features near the length scales of the employed wavelengths. Fortunately, the motion estimation largely succeeds for landfast ice, and most features in drift ice appear much easier targets for motion detection.

The different frequency bands complement each other when plentiful data is available, but they are somewhat poorer for backup purposes as each band has distinct strengths and weaknesses. On C-band, ice floe edges appear in a more reliable manner, while the L-band distinguishes the coastline better and generally shows more features and better contrast.

For motion estimation, a pair of two L-band SAR images is found to be desirable among the compared options. A pair of two C-band images also performs well, and a mixed pair performs adequately. The introduction of L-band SAR instruments can thus present both more reliable motion estimates by using L-L pairs and better time resolution, albeit at a cost of increased uncertainty, by using mixed L-C pairs.

This work provides a new tool of motion estimation to the Finnish Meteorological Institute. It also provides insights into the usage of L-band SAR images, both alone and in combination with C-band images. Thus it is good preparation for the future launch of the ALOS-2 satellite and handling its L-band images, and utilizing the GPGPU computational framework was both a strength in this work and a valuable lesson for the future.

References

ALOS User Handbook (2007). *ALOS User Handbook*. Earth Observation Research Center, Japan Aerospace Exploration Agency, 2-1-1, Sengen, Tsukuba-city, Ibaraki 305-8505 Japan.

Anandan, P. and Weiss, R. (1985). Introducing a smoothness constraint in a matching approach to optical flow fields. In *Workshop on Computer Vision, Michi*.

Arkett, M., Flett, D., De Abreu, R., Clemente-Colon, P., Woods, J., and Melchior, B. (2008). Evaluating alos-palsar for ice monitoring-what can l-band do for the north american ice service? In *Geoscience and Remote Sensing Symposium, 2008. IGARSS 2008. IEEE International*, volume 5, pages V–188. IEEE.

ASAR Product Handbook (2007). *ASAR Product Handbook*. European Space Agency, 8-10 rue Mario Nikis, 75738 Paris, Cedex 15, France.

Astola, J., Haavisto, P., and Neuvo, Y. (1990). Vector median filters. *Proceedings of the IEEE*, 78(4):678–689.

Cheng, D. K. (1993). *Fundamentals of Engineering Electromagnetics*. Prentice-Hall, Inc.

Collins, M. J. and Emery, W. J. (1988). A computational method for estimating sea ice motion in sequential seasat synthetic aperture radar imagery by matched filtering. *Journal of geophysical research*, 93(C8):9241–9251.

Dierking, W. and Busche, T. (2006). Sea ice monitoring by l-band sar: An assessment based on literature and comparisons of jers-1 and ers-1 imagery. *IEEE Transactions on Geoscience and Remote Sensing*, 44.

Dierking, W. and Haas, C. (2012). Advances of sea-ice observations since arctic 91. *Polarforschung*, 82(1):1–18.

Eicken, H., Gradinger, R., Salganek, M., Shirasawa, K., Perovich, D., and Leppï¿œranta, M. (2009). *Field Techniques for Sea Ice Research*. University of Alaska Press.

Emery, W., Fowler, C., Hawkins, J., and Preller, R. (1991). Fram strait satellite image-derived ice motions. *Journal of Geophysical Research*, 96(C3):4751–4768.

Eriksson, L. E., Borenäs, K., Dierking, W., Berg, A., Santoro, M., Pemberton, P., Lindh, H., and Karlson, B. (2010). Evaluation of new spaceborne sar sensors for sea-ice monitoring in the baltic sea. *Canadian Journal of Remote Sensing*, 36(S1):S56–S73.

Fily, M. and Rothrock, D. (1987). Sea ice tracking by nested correlations. *Geoscience and Remote Sensing, IEEE Transactions on*, (5):570–580.

Frisk, M., Komulainen, M.-L., Kotro, J., Nietosvaara, V., Tuomi, T., Johansson, M., Kahma, K., Pettersson, H., Tuomi, L., and Vainio, J. (2003). *Sää- ja meritieto*.

Hall, R. and Rothrock, D. (1981). Sea ice displacement from seasat synthetic aperture radar. *Journal of Geophysical Research: Oceans (1978–2012)*, 86(C11):11078–11082.

Horn, B. and Schunck, B. (1981). Determining optical flow. *Artificial intelligence*, 17(1-3):185–203.

Johannessen, O. M., Alexandrov, V. Y., Alexandrov, V., Frolov, I. Y., and Bobylev, L. P. (2007). *Remote Sensing of Sea Ice in the Northern Sea Route*. Praxis Publishing Limited.

Kankaku, Y., Osawa, Y., Suzuki, S., and Watanabe, T. (2009). The overview of the l-band sar onboard alos-2. In *Proceedings of Progress in Electromagnetics Research Symposium*.

Karvonen, J. (2012). Operational sar-based sea ice drift monitoring over the baltic sea. *Ocean Science*, 8:473–483.

Karvonen, J., Simila, M., and Lehtiranta, J. (2007). Sar-based estimation of the baltic sea ice motion. In *Geoscience and Remote Sensing Symposium, 2007. IGARSS 2007. IEEE International*, pages 2605–2608. IEEE.

Kim, Y. H., Martínez, A. M., and Kak, A. C. (2005). Robust motion estimation under varying illumination. *Image and Vision Computing*, 23(4):365–375.

Kwok, R., Curlander, J. C., McConnell, R., and Pang, S. S. (1990). An ice-motion tracking system at the alaska sar facility. *Oceanic Engineering, IEEE Journal of*, 15(1):44–54.

Leppäranta, M. (2011). *The drift of sea ice*. Springerverlag Berlin Heidelberg.

Leppäranta, M. and Hakala, R. (1992). The structure and strength of first-year ice ridges in the baltic sea. *Cold Regions Science and Technology*, 20(3):295–311.

Lillesand, T. M., Kiefer, R. W., and Chipman, J. W. (2004). *Remote sensing and image interpretation*. John Wiley & Sons, Inc., fifth edition.

Liu, A. K., Martin, S., and Kwok, R. (1997). Tracking of ice edges and ice floes by wavelet analysis of sar images. *Journal of atmospheric and oceanic technology*, 14:1187–1198.

Mäkynen, M. and Hallikainen, M. (2004). Investigation of c-and x-band backscattering signatures of baltic sea ice. *International Journal of Remote Sensing*, 25(11):2061–2086.

Manduchi, R. and Mian, G. A. (1993). Accuracy analysis for correlation-based image registration algorithms. In *Circuits and Systems, 1993., ISCAS'93, 1993 IEEE International Symposium on*, pages 834–837. IEEE.

Miranda, N., Duesmann, B., Pinol, M., Giudici, D., and D'Aria, D. (2010). Impact of the envisat mission extension on sar data. Technical note, European Space Agency.

Morena, L., James, K., and Beck, J. (2004). An introduction to the radarsat-2 mission. *Canadian Journal of Remote Sensing*, 30(3):221–234.

Myrberg, K., Leppäranta, M., and Kuosa, H. (2006). *Itämeren fysiikka, tila ja tulevaisuus*. Palmenia. Helsinki University Press.

Nagel, H.-H. and Enkelmann, W. (1986). An investigation of smoothness constraints for the estimation of displacement vector fields from image sequences. *Pattern Analysis and Machine Intelligence, IEEE Transactions on*, (5):565–593.

Ninnis, R., Emery, W., and Collins, M. (1986). Automated extraction of pack ice motion from advanced very high resolution radiometer imagery. *Journal of Geophysical Research*, 91(C9):10725–10.

Onstott, R. G. (1992). Sar and scatterometer signatures of sea ice. *Microwave remote sensing of sea ice*, pages 73–104.

Seifert, T., Tauber, F., and Kayser, B. (2001). A high resolution spherical grid topography of the baltic sea–2nd edition, baltic sea science congress, stockholm 25-29. november 2001, poster# 147. *Online: www. iowarnemuende. de/iowtopo*.

Seinä, A., Palosuo, E., and Grönvall, H. (1997). *Merentutkimuslaitoksen jääpalvelu 1919 - 1994*. Number 32 in MERI - Report Series of the Finnish Institute of Marine Research. Finnish Institute of Marine Research.

Sun, Y. (1994). A new correlation technique for ice-motion analysis. *EARSeL Int. J. of Advances in Remote Sensing*, 3(2):57–63.

The Baltic Sea Portal (2009). Ice winter 2008-2009.

Thomas, M. (2004). *Global motion estimation of sea ice using synthetic aperture radar imagery*. PhD thesis, Citeseer.

Thomas, M., Kambhamettu, C., and Geiger, C. (2011). Motion tracking of discontinuous sea ice. *Geoscience and Remote Sensing, IEEE Transactions on*, (99):1–16.

Tso, B. and Mather, P. M. (2009). *Classification methods for remotely sensed data*. CRC PressI Llc.

Vesecky, J. F., Samadani, R., Smith, M. P., Daida, J. M., and Bracewell, R. N. (1988). Observation of sea-ice dynamics using synthetic aperture radar images: Automated analysis. *Geoscience and Remote Sensing, IEEE Transactions on*, 26(1):38–48.

Vihma, T. and Haapala, J. (2009). Geophysics of sea ice in the baltic sea: A review. *Progress in Oceanography*, 80(3):129–148.

Weeks, W. F. and Ackley, S. F. (1986). The growth, structure, and properties of sea ice. In Untersteiner, N., editor, *The Geophysics of Sea Ice*, volume 146 of *NATO Advanced Science Institutes Series B: Physics*, chapter 1, pages 22–23. Plenum Press.

Wessel, P. and Smith, W. H. (1996). A global, self-consistent, hierarchical, high-resolution shoreline database. *Journal of Geophysical Research*, 101(B4):8741–8743.